Statistical and Dynamical Characteristics of Extreme Wave Crests Assessed with Field Measurements from the North Sea

MIKA P. MALILA,[a,b] FRANCESCO BARBARIOL,[c] ALVISE BENETAZZO,[c] ØYVIND BREIVIK,[a,b] ANNE KARIN MAGNUSSON,[a] JIM THOMSON,[d] AND BRIAN WARD[e]

[a] *Norwegian Meteorological Institute, Bergen, Norway*
[b] *Geophysical Institute, University of Bergen, Bergen, Norway*
[c] *Institute of Marine Sciences (ISMAR)–National Research Council (CNR), Venice, Italy*
[d] *Applied Physics Laboratory, University of Washington, Seattle, Washington*
[e] *AirSea Laboratory, Centre for Ocean Research and Exploration, Ryan Institute, National University of Ireland, Galway, Ireland*

(Manuscript received 7 June 2022, in final form 6 October 2022)

ABSTRACT: Wave crests of unexpected height and steepness pose a danger to activities at sea, and long-term field measurements provide important clues for understanding the environmental conditions that are conducive to their generation and behavior. We present a novel dataset of high-frequency laser altimeter measurements of the sea surface elevation gathered over a period of 18 years from 2003 to 2020 on an offshore platform in the central North Sea. Our analysis of crest height distributions in the dataset shows that mature, high sea states with high spectral steepness and narrow directional spreading exhibit crest height statistics that significantly deviate from standard second-order models. Conversely, crest heights in developing sea states with similarly high steepness but wide directional spread correspond well to second-order theory adjusted for broad frequency bandwidth. The long-term point time series measurements are complemented with space–time stereo video observations from the same location, collected during five separate storm events during the 2019/20 winter season. An examination of the crest dynamics of the space–time extreme wave crests in the stereo video dataset reveals that the crest speeds exhibit a slowdown localized around the moment of maximum crest elevation, in line with prevailing theory on nonlinear wave group dynamics. Extending on previously published observations focused on breaking crests, our results are consistent for both breaking and nonbreaking extreme crests. We show that wave crest steepness estimated from time series using the linear dispersion relation may overestimate the geometrically measured crest steepness by up to 25% if the crest speed slowdown is not taken into account.

SIGNIFICANCE STATEMENT: Better understanding of the statistics and dynamical behavior of extreme ocean surface wave crests is crucial for improving the safety of various operations at sea. Our study provides new, long-term field evidence of the combined effects of wave field steepness and directionality on the statistical distributions of crest heights in storm conditions. Moreover, we show that the dynamical characteristics of extreme wave crests are well described by recently identified nonlinear wave group dynamics. This finding has implications, for example, for wave force calculations and the treatment of wave breaking in numerical wave models.

KEYWORDS: Wave breaking; Wind waves; In situ oceanic observations; Time series

1. Introduction

The danger posed to various activities at sea by waves whose height and steepness exceed standard expectations for a given sea state has motivated extreme wave studies for decades. Various physical mechanisms—including the directional or dispersive focusing of linear wave components, wave–current interactions, and high-order nonlinear wave–wave interactions—have been proposed to explain why certain sea state conditions appear more susceptible to individual trough-to-crest wave heights H exceeding the so-called rogue wave threshold $H \geq 2H_s$, or alternatively, crest heights C exceeding the rogue crest threshold $C \geq 1.25H_s$ [see the comprehensive reviews of Dysthe et al. (2008) and Adcock and Taylor (2014)]. The exact threshold for defining an extreme or rogue wave is subject to rather arbitrary preference, with certain authors favoring higher thresholds than the ones given here in order to focus on events of lower occurrence probability (see, e.g., Cavaleri et al. 2020). Indeed, waves higher than twice the significant wave height can be expected to occur approximately daily at any point in the ocean (Dysthe et al. 2008). References to "rogue" waves or wave crests in the present text are therefore only used to distinguish measurements that exceed the aforementioned, commonly applied thresholds, which may not fully represent truly unexpected waves in a given sea state.

To evaluate the relative importance of the various proposed mechanisms in producing real-world rogue or otherwise extreme waves in realistic, open ocean conditions requires vast quantities of wave measurements in order to populate the tails of empirical wave and crest height distributions. At the time of writing, this is becoming attainable thanks to growing networks of publicly available wave observations collected by wave buoys and platforms worldwide (Christou and Ewans 2014; Cattrell et al. 2018; Häfner et al. 2021). However, the interpretation of the observational evidence is complicated by

Corresponding author: Mika P. Malila, mikapm@met.no

DOI: 10.1175/JPO-D-22-0125.1

the high wave-field directionality and broad range of wave frequencies present in the open ocean compared to the comparatively idealized wave conditions encountered in most numerical and laboratory experiments.

Measurements of rogue waves whose validity can be verified with independent observations remain relatively rare. In the comparatively few cases of verified rogue wave events, the measurements have typically been validated after their occurrence by examining the height of the damage inflicted on the observational instrumentation or the observational platform that is consistent with the measured wave heights. Examples of measured rogue wave events validated by platform damage include the 1995 New Year's wave at the Draupner platform (Haver 2004) and the extreme wave group recorded by a buoy near the FiNo platform in the southern North Sea during the 2006 Britta storm (Pleskachevsky et al. 2012). However, to date, most of the observational evidence for extreme individual waves comes from single point measurements such as wave buoys, wave staffs, or range-finding lasers, and the validity of these measurements is typically assessed based on the known dynamical properties of the sea surface (Christou and Ewans 2014; Makri et al. 2016; Cattrell et al. 2018; Voermans et al. 2021).

The Ekofisk oil and gas platform complex, located in the central part of the North Sea between Scotland and Denmark and operated by ConocoPhillips Norway, is a site containing some of the longest continuous surface wave measurements worldwide, with records starting as early as the 1980s (Krogstad et al. 2008). In the current study, long-term crest height statistics are investigated using time series of the sea surface elevation measured by a high-frequency infrared laser altimeter array (LASAR) covering storm events in the time period spanning 2003–20. The LASAR time series has been thoroughly quality controlled by a combination of despiking, following the nonparametric approach of Malila et al. (2022a), and a visual comparison of extreme wave profiles after the automated despiking. Additionally, extreme crest dynamics and space–time statistics are investigated using more recent sea surface reconstructions from a nearby stereo video system (see also Malila et al. 2022b). The observational datasets are supplemented with directional wave spectra from a recent numerical wave model hindcast for the North Sea region (NORA3; Haakenstad et al. 2021; Breivik et al. 2022).

The remainder of this article is structured as follows. Section 2 provides a review of previously published theory that is relevant for the analysis of our observational results. Section 3 describes the processing of the Ekofisk LASAR and stereo video datasets. Section 4 presents the results on (i) wave profiles and crest height statistics inferred from the long-term LASAR time series, and (ii) space–time extreme (STE) crest height characteristics inferred from the short-term stereo video space–time wave field reconstructions. Section 5 investigates the crest speed dynamics of the stereo video STE wave crests, and section 6 provides a critical discussion of our results in light of past findings. Finally, section 7 summarizes the main conclusions from the analysis.

2. Theoretical background

a. Crest statistics

1) Crest height distributions

A central topic in extreme wave investigations in the past two decades has been the identification of sea states that may lead to an increased likelihood of encountering a wave crest exceeding a certain height threshold relative to the prevailing sea state. To lowest order in wave steepness ak, the spatially homogeneous and temporally stationary sea surface $\eta(\mathbf{x}, t)$ can be represented as a linear superposition of sinusoidal wave components of random phase and amplitude,

$$\eta(\mathbf{x}, t) = \sum_{k} a(\mathbf{k}) \cos[\mathbf{k} \cdot \mathbf{x} - \omega t + \phi(\mathbf{k})], \tag{1}$$

where the wave amplitudes a and phases ϕ are stochastic variables (Tucker et al. 1984), $\mathbf{k}$ is the wavenumber vector, and $\omega = 2\pi f$ is the angular frequency. The frequency and wavenumber domains are related by the linear dispersion relationship

$$\omega^2 = gk \tanh(kd), \tag{2}$$

where $k = |\mathbf{k}|$ is the wavenumber magnitude, g is the gravitational acceleration, and d is the water depth. In the linear (i.e., Gaussian) model, statistical independence is assumed among the wave components, which prohibits energy exchange between wave components and leads wave crests C (i.e., the wave amplitudes for narrow-banded sinusoidal waves) to follow the Rayleigh exceedance probability distribution:

$$P_R(C/H_s > z) = \exp(-8z^2). \tag{3}$$

Here $H_s = 4\sqrt{m_{000}}$ is the significant wave height and m_{000} is the zeroth-order moment of the wave spectrum, which approximates the sea surface variance σ^2 (see, e.g., Holthuijsen 2007). The spectral moments m_{ijl} of the two-dimensional frequency-directional wave spectrum $E(\omega, \theta)$ are defined by

$$m_{ijl} = \int_0^{2\pi} \int_0^{\infty} k_x^i k_y^j \omega^l E(\omega, \theta)\, d\omega\, d\theta. \tag{4}$$

It has long been accepted that the linear representation of sea surface displacements leads to an underestimation of the exceedance probability of large crest heights in realistic sea states (Longuet-Higgins 1963). The leading-order cause for this underestimation is the weak nonlinearity (i.e., wave–wave energy exchange) inherent in ocean waves, which manifests itself as slightly higher crests and shallower troughs compared to purely sinusoidal (i.e., linear) wave forms. However, this weak nonlinearity—represented mathematically by a perturbation expansion of Eq. (1) to second order in wave steepness—has a rather small effect on the crest-to-trough wave heights (Tayfun and Fedele 2007). Second-order (also known as bound-wave) effects have been incorporated into crest height distributions by Forristall (2000) in the form of a Weibull-type distribution:

$$P_F(C/H_s > z) = \exp\left[-\left(\frac{z}{\alpha_F}\right)^{\beta_F}\right], \tag{5}$$

where $\alpha_F = 0.3536 + 0.2568\epsilon_F + 0.0800U_{rs}$ and $\beta_F = 2 - 1.7912\epsilon_F - 0.5302U_{rs} + 0.2824U_{rs}^2$, and $\epsilon_F = (2\pi/g)(H_s/T_m^2)$ is a measure of the wave steepness, with the mean wave period $T_m = m_{000}/m_{001}$. The term $U_{rs} = H_s/(k_m^2 d^3)$ is the Ursell number, which describes the effect of water depth on nonlinearity. The mean wavenumber k_m is estimated from the mean period T_m using the linear dispersion relation. For $\epsilon_F = 0$ and $U_{rs} = 0$, the Forristall distribution collapses to the Rayleigh distribution in Eq. (3).

Another commonly used second-order distribution is given by Tayfun (1980) as

$$P_T(C/H_s > z) = \exp\left[-\frac{1}{2\epsilon_{FT}^2}\left(\sqrt{1 + 8\epsilon_{FT}z} - 1\right)^2\right], \tag{6}$$

where

$$\epsilon_{FT} = \sqrt{m_{000}}\,\frac{(2\pi m_{001}/m_{000})^2}{g}(1 - \nu + \nu^2) \tag{7}$$

is the Fedele and Tayfun (2009) spectral steepness parameter for broad-banded sea states, in which $\nu = \sqrt{m_{000}m_{002}/m_{001}^2 - 1}$ is a measure of the spectral frequency bandwidth (Longuet-Higgins 1975). In deep water, where U_{rs} tends to zero, both the Forristall and Tayfun distributions are solely dependent on the leading-order parameter controlling wave nonlinearity, namely the bulk wave steepness.

2) MAXIMUM CREST HEIGHT DISTRIBUTIONS IN SPACE AND TIME

The crest height exceedance probability distributions mentioned above are valid for one-dimensional time series measurements at one point in space in statistically stationary, long-crested sea states. In realistic, short-crested and evolving sea states, the time series approach is known to underestimate the height of the largest crests for two main reasons, as discussed by Fedele (2012). First, at any instant in time, a randomly located point is unlikely to measure the highest crest elevation in a given finite area. Second, the wave group structure is known to evolve both spatially and temporally, so a fixed point in space is also unlikely to capture a wave crest at the wave group apex (also called the wave group focusing point) in both space and time (see Boccotti 2000).

To account for the increased probability of encountering large crest elevations when considering a sea surface area rather than a fixed point, Fedele (2012) extended the linear Rayleigh crest height distribution [Eq. (3)] to three dimensions (the two-dimensional sea surface and time) following the theoretical framework of time-evolving Gaussian fields of Baxevani and Rychlik (2006) and Adler and Taylor (2007). Fedele (2012) and Fedele et al. (2013) showed that the resulting linear exceedance probability for space-time maximum crests within a space–time volume of size XYD, where X and Y define the spatial extent and D defines the time duration, can be approximated by

$$P_{R,3D}[C_{\max}/H_s > z|(N_V, N_S, N_B)] \approx \left(32\pi N_V z^2 + 4\sqrt{2\pi}N_S z + N_B\right)P_R, \tag{8}$$

where N_V, N_S, and N_B represent the average number of waves in the 3D space–time volume (V), on the outer 2D surface of the volume (S) and on the 1D boundaries of the surface (B), respectively. These parameters can be estimated from the wave spectrum by the following expressions (Fedele 2012):

$$N_V = \frac{XYD}{L_x L_y T_{m_{02}}}\sqrt{1 - \alpha_{xt}^2 - \alpha_{yt}^2 - \alpha_{xy}^2 + 2\alpha_{xt}^2\alpha_{yt}^2\alpha_{xy}},$$

$$N_S = \frac{XD}{L_x T_{m_{02}}}\sqrt{1 - \alpha_{xt}^2} + \frac{YD}{L_y T_{m_{02}}}\sqrt{1 - \alpha_{yt}^2} + \frac{XY}{L_x L_y}\sqrt{1 - \alpha_{xy}^2},$$

$$N_B = \frac{X}{L_x} + \frac{Y}{L_y} + \frac{D}{T_{m_{02}}}. \tag{9}$$

In Eq. (9), L_x, L_y, and $T_{m_{02}}$ (the wavelength, the crest length, and the mean wave period), are estimated from the 3D spectral moments defined in Eq. (4) such that $L_x = 2\pi\sqrt{m_{000}/m_{200}}$, $L_y = 2\pi\sqrt{m_{000}/m_{020}}$, and $T_{m_{02}} = \sqrt{m_{000}/m_{002}}$. The parameters α_{xt}, α_{yt}, and α_{xy} characterize the irregularity of the sea state in space and time, and are defined as

$$\alpha_{xt} = \frac{m_{101}}{\sqrt{m_{200}m_{002}}}, \quad \alpha_{yt} = \frac{m_{011}}{\sqrt{m_{020}m_{002}}}, \quad \alpha_{xy} = \frac{m_{110}}{\sqrt{m_{200}m_{020}}}. \tag{10}$$

Nonlinear effects to second order in wave steepness were incorporated into the 3D extension of maximum crest height exceedance probability distributions by Benetazzo et al. (2015), who approximated the 3D-expanded Tayfun distribution [Eq. (6)] as

$$P_{T,3D}[C_{\max}/H_s > \xi|(N_V, N_S, N_B)] \approx (N_V z^2 + N_S z + N_B)P_R. \tag{11}$$

Here, $\xi = z + (2\epsilon_{FT})z^2$ is the second-order normalized crest height following Tayfun (1980).

3) NONLINEARITY PARAMETERS

For representing the degree of wave field nonlinearity with statistical parameters, a large body of literature has focused on higher-order statistical moments of surface displacement time series such as the skewness,

$$\gamma = \frac{\mu_3}{\sigma^3}, \tag{12}$$

and kurtosis,

$$\kappa = \frac{\mu_4}{\sigma^4}, \tag{13}$$

where μ_n is the nth central moment of η and σ is its standard deviation (Janssen 2003; Mori and Janssen 2006; Mori et al. 2007, 2011). Departures of the skewness and kurtosis from their known values for a Gaussian distribution of 0 and 3,

respectively, are generally taken as indicators for the presence of nonlinear effects. From a related viewpoint, γ and κ are measures of the thickness of the high-end tail of wave and crest height distributions.

It has been shown that in certain idealized wave conditions, including infinite water depth, narrow spectral bandwidth, and narrow directional spreading, the wave spectrum $E(f, \theta)$ is susceptible to exponential growth of side-band perturbations, which can lead to a dramatic redistribution of the wave energy within a wave group such that the amplitude of one wave (typically the central wave of the group) grows rapidly at the expense of the others (Benjamin and Feir 1967). This physical mechanism is known as modulational instability, and has been proposed as a potential process responsible for extreme wave generation in the ocean (Dysthe et al. 2008). The modulational instability is known to increase in strength as the ratio of spectral steepness to spectral width (known as the Benjamin–Feir index) grows large, implying that the nonlinear energy focusing effects of wave steepness outweigh the dispersive effects of finite bandwidth (Janssen 2003). Following Serio et al. (2005), the Benjamin–Feir index (BFI) is defined as

$$\mathrm{BFI} = \sqrt{m_{000}} k_m Q_p \sqrt{2\pi} \mu \sqrt{\frac{|\beta|}{\alpha}}, \tag{14}$$

where μ, α, and β, correction parameters for finite depth and nonlinearity, are specified in Serio et al. (2005). The spectral width is represented by the spectral peakedness parameter of Goda (1970):

$$Q_p = \frac{2}{m_{000}^2} \int_0^\infty f E^2(f) df. \tag{15}$$

Equation (14) also contains a measure of the spectral steepness,

$$\epsilon = \sqrt{2 m_{000}} k_m, \tag{16}$$

which will be used hereafter to quantify the bulk steepness of a sea state in our field datasets unless another definition is specified. The spectral steepness is known to be closely related to the skewness of the sea surface (Tayfun 1980). For narrow-band sea states, this relation can be expressed following Fedele and Tayfun (2009) as

$$\gamma = \frac{3\epsilon}{\sqrt{2}}, \tag{17}$$

where the $\sqrt{2}$ follows from the spectral steepness definition $\epsilon_{FT,N} = \sqrt{m_{000}} k_m = \epsilon/\sqrt{2}$ employed by Fedele and Tayfun (2009).

The resonance criteria for modulational instability are strongly constrained by the directionality of a wave field. Gramstad and Trulsen (2007) showed with numerical simulations of the nonlinear Schrödinger equation—an equation that governs the dynamics of nonlinear water waves—that wave height statistics begin to significantly deviate from the Rayleigh distribution only for long-crested sea states with crest lengths approximately 10 times longer than the dominant wavelength. The moderating effects of increased directional spreading on modulational instability were subsequently included in the BFI parameter by Mori et al. (2011), who defined a two-dimensional Benjamin–Feir index as

$$\mathrm{BFI}_{2\mathrm{D}}^2 = \frac{\mathrm{BFI}^2}{1 + \alpha_2 R}, \tag{18}$$

where $\alpha_2 = 7.1$ is an empirical coefficient and R is a parameter that represents the ratio of directional spreading σ_θ to frequency bandwidth, defined as

$$R = \frac{\sigma_\theta}{2\nu}, \tag{19}$$

where the spectral bandwidth ν is inversely related to Q_p (Longuet-Higgins 1975). A sea state is considered to be in a regime favorable to nonlinear energy focusing if $0 \leq R < 1$ (Janssen and Bidlot 2009).

Following from the assumptions behind the theory of modulational instability, Janssen (2003) proposed that there exists a functional relationship between a narrowband, random wave field's BFI and its kurtosis. This assumption was further elaborated by Mori and Janssen (2006), who derived the relation

$$\kappa = \frac{\pi}{\sqrt{3}} \mathrm{BFI}^2 \tag{20}$$

to represent the impact on the kurtosis by the competing effects of wave-field nonlinearity (i.e., steepness) and dispersion (i.e., spectral width). A similar relation was introduced for directional wave fields by Mori et al. (2011) by

$$\kappa = \frac{\pi}{\sqrt{3}} \mathrm{BFI}_{2\mathrm{D}}^2. \tag{21}$$

When third-order nonlinear effects, including modulational instability, are taken into account, the kurtosis is commonly decomposed into second-order contributions by bound waves (κ_b) and dynamic contributions (κ_d) (Janssen 2009). The bound contribution for narrow-band, deep water waves is then defined following Janssen and Bidlot (2009) as

$$\kappa_b = 18 \frac{\epsilon}{\sqrt{2}}. \tag{22}$$

Approximate upper and lower bounds, $\kappa_{d,\max}$ and $\kappa_{d,\min}$, for the dynamic contribution due to nonlinear wave–wave interactions in directional wave fields with $0 \leq R < 1$ were given by Fedele (2015):

$$\kappa_{d,\max} \approx \frac{b}{(2\pi)^2} \frac{1 - R}{R + bR_0}, \tag{23}$$

where $b = 2.48$, $R_0 = 3\sqrt{3}/\pi$, and

$$\kappa_{d,\min} = -R\kappa_{d,\max}. \tag{24}$$

It has been shown with laboratory and numerical wave tank experiments that in wave field conditions prone to modulational instability, the probability of occurrence of extreme crest heights is

significantly elevated over linear and second-order predictions (Dysthe et al. 2003; Toffoli et al. 2010b; Støle-Hentschel et al. 2018). However, a number of recent publications based on wave and crest height measurements taken in the field cast doubt on the notion that the required conditions regarding the combination of wave steepness and spectral narrowness (in both frequency and direction) are realistically attainable in the real ocean (Christou and Ewans 2014; Cattrell et al. 2018; Häfner et al. 2021). Consequently, the prevailing theory expects extreme crests to occur primarily as a result of linear directional and dispersive focusing combined with second-order, bound wave amplification, with infrequent contributions from higher-order nonlinear effects (Gemmrich and Garrett 2011; Trulsen et al. 2015; Fedele et al. 2016, 2019; Benetazzo et al. 2021; Gemmrich and Cicon 2022). It may also be noted that Dematteis et al. (2019) have recently suggested a theoretical framework based on so-called hydrodynamic instantons, which may be able to explain extreme wave and wave crest formation and likelihood by any physical mechanism to high accuracy.

b. *Crest dynamics*

1) Breaking-limited wave steepness

While increased wave steepness affects crest height statistics through amplified nonlinear wave-wave interaction, the shape and size of extreme waves in the open ocean is to a large extent also constrained by wave steepness. Intuitively, the wave steepness grows as a wave becomes higher or shorter, or both, ultimately leading to wave breaking as a critical steepness threshold is exceeded (Perlin et al. 2013). Dynamically, the recent, unified wave breaking framework of Barthelemy et al. (2018) holds that the initiation of wave breaking depends on the ratio of the wave crest energy flux to the energy density, normalized by the local crest speed.

In the bulk sense, Zippel and Thomson (2017) found significant wave heights H_s in an intermediate-depth river inlet environment to be effectively bounded by the threshold

$$\frac{H_s k_m}{\tanh(k_m d)} = 0.4, \tag{25}$$

where the denominator on the left-hand side makes the expression valid for arbitrary water depth. For individual waves of height H and local wavenumber k in arbitrarily deep water, the limiting wave steepness is given by Miche (1944) for ideal nonlinear Stokes waves (Stokes 1847) as

$$\frac{Hk}{\tanh(kd)} = \frac{2\pi}{7}. \tag{26}$$

The approximate validity of the Stokes–Miche limit as an upper bound for wave steepness has been verified by observational datasets collected in shallow (Power et al. 2010; Carini et al. 2021), intermediate (Saket et al. 2018; Mendes et al. 2021), and deep water (Christou and Ewans 2014); however, notably, Toffoli et al. (2010a) found that the limiting wave front steepness of actively breaking waves may locally exceed the limit implied by Eq. (26) by up to 25%. Nevertheless, more recent field observations support the validity of the limiting Stokes (1847) profile as an upper bound for the steepness of actively breaking waves in the ocean (Schwendeman and Thomson 2017).

The degree of directional spreading of the wave energy in a specific sea state is believed to significantly impact the breaking characteristics of the largest crests. Analyzing a large dataset of wave tank measurements, Latheef and Swan (2013) found an intricate balance between the competing effects of nonlinear amplification and breaking-induced reduction in high-crest height probabilities in deep-water, high-steepness sea states under varying ranges of directional spread. They observed sea states characterized by broad directional spread (i.e., short-crested wave fields) allowing the largest crests to grow higher before breaking. Conversely, nonlinear crest-height amplifying effects beyond second order were strongest for sea states with narrow directional spread (i.e., long-crested wave fields) and high, though not extreme, steepness. Similar results were more recently reported in intermediate water depth by Karmpadakis et al. (2019).

Recently, a number of studies have focused on the effects of crossing sea states on wave breaking and its implications for wave and crest height distributions. McAllister et al. (2019) showed with laboratory experiments that crossing seas with high separation angles between wave systems affected the breaking characteristics of the largest crests in a way that allowed higher maximum crest elevations compared to situations with smaller crossing angles. Crossing seas with approximately equal energy density in the two systems has also been shown in numerical simulations to potentially enhance both linear focusing and nonlinear wave-wave interactions at certain crossing angles, which may have consequences for the tails of crest height distributions in such sea states (Donelan and Magnusson 2005; Cavaleri et al. 2012; Gramstad et al. 2018; Benetazzo et al. 2021). In the present study, however, we focus our analysis of crest height statistics on predominantly unimodal, wind-sea-dominated sea states for which, for example, the sea state steepness is comparatively straightforward to define from a one-dimensional frequency spectrum.

2) Crest speed dynamics at finite wave steepness

Until relatively recently, field observations of both wave statistics and dynamics were almost exclusively collected with instruments producing time series at one point in space, such as wave buoys or range-measuring devices including laser altimeters. To infer dynamically important properties such as wave steepness (a geometric quantity) from time series measurements generally relies on the validity of the linear dispersion relation, Eq. (2), or a higher-order approximation thereof. In the past decade, high-resolution wave field reconstruction in three dimensions (the two-dimensional spatial sea surface and time) using stereo video imagery has become increasingly popular thanks to its low-cost equipment requirements and the release of targeted open source software (Benetazzo 2006; Bergamasco et al. 2017; Schwendeman and Thomson 2017; Vieira et al. 2020). Measurements that resolve the spatial dimension in addition to time allow for the direct measurement of geometric wave profiles, and provide the opportunity to validate geometric and dynamic wave characteristics without resorting to the dispersion relation.

The theory of Stokes (1847) for steady, nonlinear water waves predicts an increase of the wave phase speed with increasing wave steepness. To second order in wave steepness, the phase speed $c = \omega/k$ is given as

$$c = c_0[1 + (ak)^2], \tag{27}$$

where c_0 is the linear phase speed conforming to Eq. (2). However, the crest dynamics of realistic, nonlinear wave groups are known to be influenced by both nonlinearity (contributing to crest acceleration) and dispersion (contributing to crest deceleration), leading to a net crest slowdown due to the time- and space-varying profile evolution experienced by individual carrier waves as the wave group envelopes attain their maximum local amplitude and, consequently, steepness (Tayfun 1986; Banner et al. 2014). A local crest speed slowdown of $\mathcal{O}(20\%)$ compared to c_0 has been observed in previous stereo video field measurements of breaking waves by Banner et al. (2014) and Schwendeman and Thomson (2017), suggesting that wave breaking is preferably initiated at the focal point (in time and space) of wave group evolution (see also Malila et al. 2022b). This slowdown is hypothesized to contribute to the peak location of breaking crest length distributions, $\Lambda(c)$ in the framework of Phillips (1985), often observed at values of c somewhat lower than the spectral peak phase speed c_p (Thomson and Jessup 2009; Kleiss and Melville 2010; Gemmrich et al. 2013).

Since measurements of extreme (e.g., rogue) waves are generally assumed to represent local wave group focal points (Boccotti 2000), it is to be expected that the slowdown applies to extreme crest dynamics in general, regardless of whether or not the crests are breaking. This may in turn affect estimates of extreme wave steepness inferred from point time series using dispersion alone. Furthermore, an accurate estimate of the local crest speed at wave group focus is critical in the breaking initiation framework of Barthelemy et al. (2018).

3. Data and methods

a. *LASAR despiking and quality control*

The laser altimeter array (LASAR) was installed in 2003 under the consultation of M. A. Donelan (University of Miami) and A. K. Magnusson (Norwegian Meteorological Institute) in the center of a footbridge connecting two bottom-mounted platforms (named 2/4-B and 2/4-K), at a distance of approximately 23 m from the 2/4-K platform. Spaced 2.6 m apart in a square configuration, each altimeter is of model Optech Sentinel 3100. The altimeters measure the distance to the instantaneous sea surface with 80 infrared (905 nm wavelength) pulses fired at 2 kHz in 40-ms intervals, which are subsequently averaged by built-in processing and converted into range readings at a final sampling frequency of 5 Hz. The sampling of each laser is offset in time by 45 ms to minimize interference between pulses from the different altimeters.

The quality of the return signal is sensitive to the reflecting properties of the sea surface. A relatively smooth sea surface may lead to specular reflection where the return signal is not received by the instrument, leading to missing range measurements. Conversely, a rough sea surface resulting from, for example, widespread wave breaking typically leads to more reliable reflection and higher-quality range measurements (Magnusson and Donelan 2013). The infrared pulse wavelength is also sensitive to sea spray aerosols, which may cause spurious reflection leading to spikes in the range measurement time series (Toffoli et al. 2011).

Due to the factors mentioned above, the raw LASAR signals frequently suffer from missing and faulty range readings, especially in calm sea states with low surface roughness leading to specular sea surface reflecting properties. This noise contamination has prevented the exploitation of the full time series for extreme wave analysis; a number of studies have, however, analyzed short storm events, which can be more readily quality controlled by visual inspection (Magnusson and Donelan 2013; Donelan and Magnusson 2017).

We have quality controlled the full LASAR time series from its beginning in February 2003 until November 2020, when the lasers were taken out of commission for maintenance, using a nonparametric despiking methodology developed to address the specific noise characteristics of laser altimeter wave measurements (Malila et al. 2022a). The despiking methodology uses Gaussian process (GP) regression to estimate a mean signal with uncertainty bounds based on raw, potentially noise-contaminated, wave signals. The GP uncertainty bounds are used to both detect unphysical spikes and to avoid the erroneous removal of real extreme wave crests. Moreover, the GP mean signal can be used to interpolate over short intervals of missing data.

As demonstrated by Malila et al. (2022a) with real example wave records from the Ekofisk LASAR time series, the GP method is highly effective in cleaning up noisy wave records, while leaving high and steep extreme waves (which often get flagged as spikes by automated despiking routines) intact. The major limitation of the GP methodology is the high computational cost of GP regression applied to large datasets, which restricts the amount of data that can be processed in one batch, and also limits the number of spike-detection and spike-replacement iterations.

As suggested by Malila et al. (2022a), we use the coefficient of determination r^2 of the GP regression fit as a proxy for the signal-to-noise ratio of the laser signals. The individual laser signals are despiked in batches of 20-min length, and if r^2 for the GP regression fit to a certain batch remains below a predefined threshold (defined here as $r^2 = 0.95$) after three despiking and spike-replacement iterations, the entire 20-min batch is discarded from further analysis. Moreover, 20-min batches containing consecutive intervals of missing data longer than 2 s and batches in which more than 10% of total data points are missing are also discarded.

Following the automated despiking procedure, we have performed a visual control by comparing the wave profiles of all rogue waves ($H \geq 2H_s$) and rogue wave crests ($C \geq 1.25H_s$) recorded by the four laser altimeters against one another. Since the measurements are essentially collocated (for sufficiently energetic sea states) and simultaneous, and because spikes appear largely randomly distributed in the signals, the

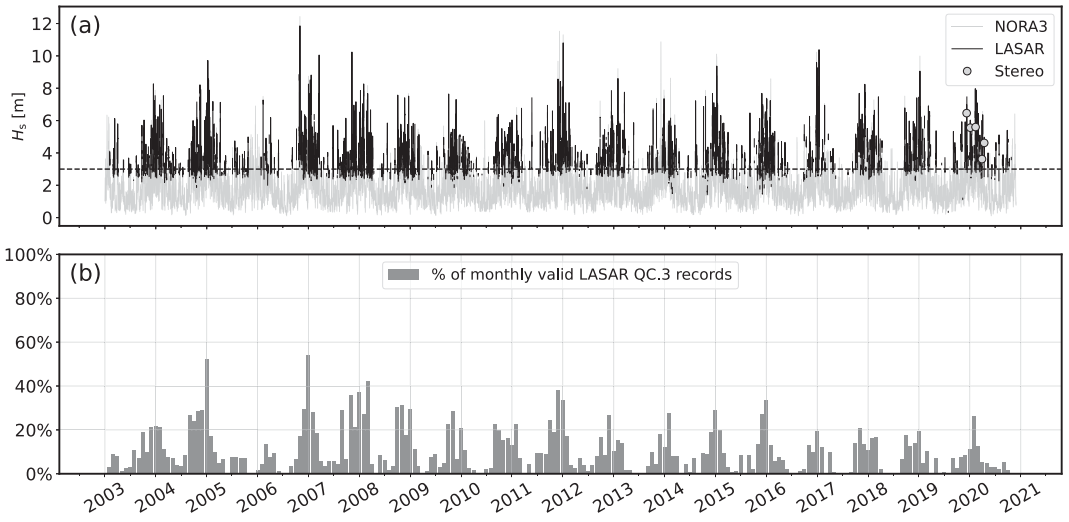

FIG. 1. (a) In gray, time series of hourly significant wave height from the NORA3 wave model hindcast (nearest grid cell to the Ekofisk coordinates). In black, time series of hourly mean H_s estimated from the four collocated laser altimeters at the Ekofisk observatory (LASAR). Only 20-min wave records that have passed the quality control at level QC.3 are included, which explains the gaps in the time series, as well as the low number of observations at $H_s < 3$ m (dashed line). The circles show the date-wise mean H_s estimates from the stereo video acquisitions (see also Table 1). (b) The number of 20-min QC.3-level LASAR records from at least one of the four laser altimeter as a percentage of hours per month.

individual laser records can be viewed as independent measurements which, when plotted together, readily distinguish erroneous measurements from valid wave profiles. The entire quality control (QC) procedure results in end products with various degrees of processing, as summarized below.

R: Raw 5-Hz range measurements. The raw measurements are inverted to sea surface elevation measurements $\eta(t)$ by subtraction of the 20-min wave record mean.

QC.0: Raw signals after an initial removal of very large-amplitude spikes using a fixed threshold of 10 median absolute deviations above and below the 20-min mean sea level [see Malila et al. (2022a) for details]. Removed spikes or original dropouts have not been replaced by interpolation.

QC.1: Result of despiking with GP regression. Removed spikes or dropouts have not been replaced by interpolation.

QC.2: As in QC.1, but with removed spikes and dropouts shorter than 2 s replaced by interpolation with the GP mean function.

QC.3: The highest level of quality control, where all QC.2-level LASAR records flagged as containing rogue waves or rogue crests have been manually verified. Individual records in which flagged rogue waves/crests turned out to be undetected spikes have been discarded. In total, approximately 3.5% of the QC.2-level records were discarded as a result of the QC.3-level control.

In the current paper, only QC.3-level LASAR records are analyzed. As seen in Fig. 1, the quality control effectively filters out LASAR measurements collected in low sea states with H_s less than approximately 3 m. We believe this largely reflects the dependence of reflected laser signal quality on sea surface roughness. To take advantage of the maximum amount of high-quality LASAR data, we hereafter use any of the available QC.3-level 20-min records with $H_s \geq 3.0$ m. However, only one laser altimeter signal per 20-min time interval is used. Based on the individual properties of the four laser altimeters (see Malila et al. 2022a), we prioritize measurements from laser number 2, which has been found to suffer the least from missing or low quality data. If a QC.3-level record for laser 2 is unavailable, the remaining order of priority is laser number 1, followed by laser 3 and, finally, laser 4.

In Fig. 1a, the H_s estimates from LASAR are plotted alongside hourly H_s estimates from the nearest grid cell in the NORA3 hindcast (Haakenstad et al. 2021; Breivik et al. 2022). The H_s estimates from LASAR and NORA3 were found to be well correlated, as described by the correlation coefficient (Pearson) $r_P = 0.915$.

The NORA3 hindcast is a combined atmospheric–wave model hindcast covering the 1998–2020 period for the North Sea, Norwegian Sea, and Barents Sea regions. The atmospheric component is generated by downscaling the global reanalysis ERA5 (Hersbach et al. 2020) using the nonhydrostatic HARMONIE-AROME atmospheric model (Haakenstad et al. 2021). The 10-m wind field is then used to force the wave hindcast, generated with a WAM cycle 4.7 spectral wave model (WAMDI Group 1988), similar to the one run operationally by the Norwegian Meteorological Institute. The wave model component of NORA3 has a 3-km grid resolution, and the publicly available output contains hourly directional wave spectra (30 frequency bands and 24 directional bands) for a number of locations of interest, including Ekofisk (Breivik et al. 2022). Since the LASAR measurements only provide one-dimensional time series and frequency spectra $E(f)$, we hereafter use the two-dimensional frequency–direction spectra $E(f, \theta)$ from NORA3 to

TABLE 1. Date-wise averaged significant wave height $\langle H_s \rangle$, mean wave period $\langle T_m \rangle$, and spectral steepness $\langle \epsilon \rangle$ from 20-min periods with stereo video acquisitions during the 2019/20 winter and spring seasons. The abbreviations stand for LASAR (L), WASS stereo video reconstructions (S), and hourly output from the NORA3 wave model hindcast (N).

	$\langle H_s \rangle$ (m)			$\langle T_m \rangle$ (s)			$\langle \epsilon \rangle$		
Date	L	N	S	L	N	S	L	N	S
9 Dec 2019	6.61	6.36	6.46	8.72	8.97	8.88	0.12	0.11	0.12
4 Jan 2020	5.67	4.92	5.56	9.54	8.73	9.24	0.09	0.09	0.09
11 Feb 2020	5.41	5.24	5.60	8.00	7.50	8.01	0.12	0.13	0.12
28 Mar 2020	3.51	3.41	3.62	6.35	6.05	6.39	0.12	0.13	0.12
13 Apr 2020	4.72	4.15	4.62	8.60	8.29	8.54	0.09	0.09	0.09

approximate the directionality of the sea states in the LASAR dataset.

b. *WASS stereo video reconstruction*

The Ekofisk stereo video cameras are located on the northwest-facing side of the 2/4-K platform, approximately 100 m to the north of the LASAR system. Details of the setup and processing of the stereo video dataset are given by Malila et al. (2022b), and will only briefly be summarized here.

The stereo video dataset contains 29 twenty-minute sea surface reconstructions processed with the open source Wave Acquisition Stereo System (WASS) software (Benetazzo et al. 2012; Bergamasco et al. 2017). The 3D point clouds returned by WASS were gridded by bilinear interpolation into georeferenced (x, y) grids for the analysis. Relevant 1D average spectral parameters for the stereo video acquisition records—namely the significant wave height H_s, the mean wave period T_m, and the spectral steepness ϵ—are presented in Table 1, in which the WASS estimates are compared against NORA3 and collocated measurements from LASAR. The WASS stereo video parameters are averages evaluated from 1D spectra estimated at 69 separate "virtual buoys" (i.e., time series at selected grid points) within the reconstructed footprint. The various estimates are found to agree with good accuracy in the relatively wide range of sea state conditions encountered during the stereo video acquisitions.

In Table 2, selected average 2D spectral parameters from frequency–directional spectral estimates are compared for the separate acquisition dates between the WASS reconstructions and NORA3, as well as WAMOS spectra (Reichert et al. 1999) from an X-band marine radar situated on the helideck of the 2/4-K platform directly above the cameras (at approximately 55 m above mean sea level). Because the limited size of the reconstructed footprint does not allow for the full spatial resolution of all wave scales, the 2D spectra from the stereo video reconstructions were estimated from heave estimates from virtual buoys with the maximum entropy method (MEM) (Lygre and Krogstad 1986) implemented in the Directional Wave Spectra (DIWASP) Matlab toolbox (Johnson 2002). Distinct variability is observed in the directional parameters estimated from the different sources. Most notably, the stereo video spectra are noticeably wider than NORA3 and WAMOS in energy-weighted mean directional spread σ_θ, defined following Kuik et al. (1988) as

$$\sigma_\theta^2 = \left\{1 - \sqrt{\left[\frac{\int \sin(\theta) E(\omega,\theta) d\omega d\theta}{\int E(\omega,\theta) d\omega d\theta}\right]^2 + \left[\frac{\int \cos(\theta) E(\omega,\theta) d\omega d\theta}{\int E(\omega,\theta) d\omega d\theta}\right]^2}\right\}. \tag{28}$$

The wave and crest lengths L_x and L_y, estimated from the 3D spectral moments defined in Eq. (4), also display significant variability between the various sources. These differences may be in part explained by the different directional resolutions of the various 2D spectral estimates. The standard WAMOS product has a directional resolution of 4°, while the MEM stereo video and NORA3 spectra have 12° and 15° directional resolutions, respectively. In certain cases, especially during the stereo video acquisitions performed on 28 March 2020, we found the spectral energy in the original WAMOS spectra to be concentrated on very narrow directional bands, which led to exaggerated estimates of the crest length L_y. For this reason, the WAMOS spectral parameters in Table 2 are computed from spectra for which the directional resolution has been coarsened by averaging into 12°. Finally, it is worth highlighting that good consistency is found in the estimates of mean wave direction θ_m (direction of wave propagation in the meteorological angle convention) among the various spectral sources.

All spectral products considered here have certain limitations. The observed spectra from WASS and WAMOS are limited not only in their temporal coverage, but the stereo video system specifically also suffers from limited spatial coverage. Due to the open-ocean location of the Ekofisk platform, the sea states commonly (and in all but the 28 March 2020 record in our acquisitions) contain dominant wave components whose wavelengths exceed the overlapping footprint of the stereo cameras. The

TABLE 2. Average directional wave parameters during the stereo video acquisitions (see also Table 1) from the NORA3 hindcast (N) and the collocated WASS stereo video (S) and WAMOS (W) 2D spectral estimates.

	$\langle L_x \rangle$ (m)			$\langle L_y \rangle$ (m)			$\langle \sigma_\theta \rangle$ (°)			$\langle \theta_m \rangle$ (°)		
Date	N	S	W	N	S	W	N	S	W	N	S	W
9 Dec 2019	86.64	94.07	67.04	105.96	93.90	94.97	29.89	48.97	31.86	161.05	163.00	161.61
4 Jan 2020	76.60	99.67	76.56	87.46	112.36	82.52	36.54	46.42	39.76	146.68	151.25	147.80
11 Feb 2020	65.13	92.71	102.79	77.28	101.95	96.41	36.05	44.79	32.44	88.54	75.97	82.15
28 Mar 2020	45.38	61.23	52.62	56.09	73.55	65.68	31.75	49.99	29.33	175.25	179.97	174.79
13 Apr 2020	69.10	81.19	50.04	81.70	96.03	69.23	26.16	43.47	29.39	173.91	174.58	172.05

veracity of the directional spectra estimated from these limited areas is therefore necessarily compromised. The NORA3 hindcast spectra are largely constrained by the accuracy of the nonhydrostatic atmospheric forcing applied in the model runs. These constraints, combined with the large variability among the spectral parameters listed in Table 2, led us to exclusively use NORA3 spectra for estimating the directional sea-state properties in the remainder of this study, including the space–time extreme analysis presented in section 4d. This ensures that directional properties are consistent between the long-term LASAR analysis and the short-term stereo video analysis.

4. Extreme crest shapes and statistics

a. *LASAR extreme wave profiles*

The visually validated profile of each individual wave in the LASAR dataset whose crest height C or trough-to-crest wave height H exceeds the commonly applied rogue wave threshold $C \geq 1.25H_s$ or $H \geq 2.0H_s$, where H_s is the significant wave height of the 20-min sea state during which the wave is observed, is plotted in Fig. 2 alongside corresponding ensemble-averaged profiles. In total, the dataset of approximately 7 million individual waves contains 601 rogue crests, 557 downward zero-crossing (DZC) rogue waves, and 631 upward zero-crossing (UZC) rogue waves. The average rogue crest profile (Fig. 2a) exhibits a pronounced symmetry around the maximum crest, with preceding and following troughs of approximately equal depth. The average DZC (Fig. 2b) and UZC (Fig. 2c) rogue wave profiles exhibit essentially mirrored asymmetry, with the DZC (UZC) crest being preceded (followed) by a somewhat shorter wave with a deep following (preceding) trough and followed (preceded) by a longer wave with a shallower trough. While the asymmetric and mirrored rogue wave profiles naturally follow from the wave height definition used (i.e., DZC or UZC), it is notable that UZC rogue waves are approximately 13% more numerous than DZC rogue waves in the LASAR dataset. This may be explained by the observation of Toffoli et al. (2010a) that actively breaking waves tend to experience a steepening of the wave front consistent with the shape of the average DZC rogue wave profile in Fig. 2b. Consistent observations on breaking versus nonbreaking temporal extreme wave profiles have been recently reported by Karmpadakis and Swan (2020). Consequently, DZC rogue waves may be less common because their profile implies ongoing breaking, with a resulting reduction of the wave amplitude.

In Fig. 3, we examine the validity of previously reported maximum steepness limits using the LASAR and stereo video field datasets. As shown in Fig. 3a, the majority of the 20-min sea states included in both the LASAR and stereo video datasets remain bounded by the bulk steepness threshold in Eq. (25); however, LASAR sea states corresponding to approximately the highest percentile in spectral steepness exceed the threshold. In Figs. 3b and 3c, the highest DZC and UZC wave heights in each sea state are compared against local wavenumbers k_z estimated from zero-crossing wave periods by the linear dispersion relation. The limiting individual-wave steepness threshold of Miche (1944) [Eq. (26)] is shown to effectively bound the individual maximum

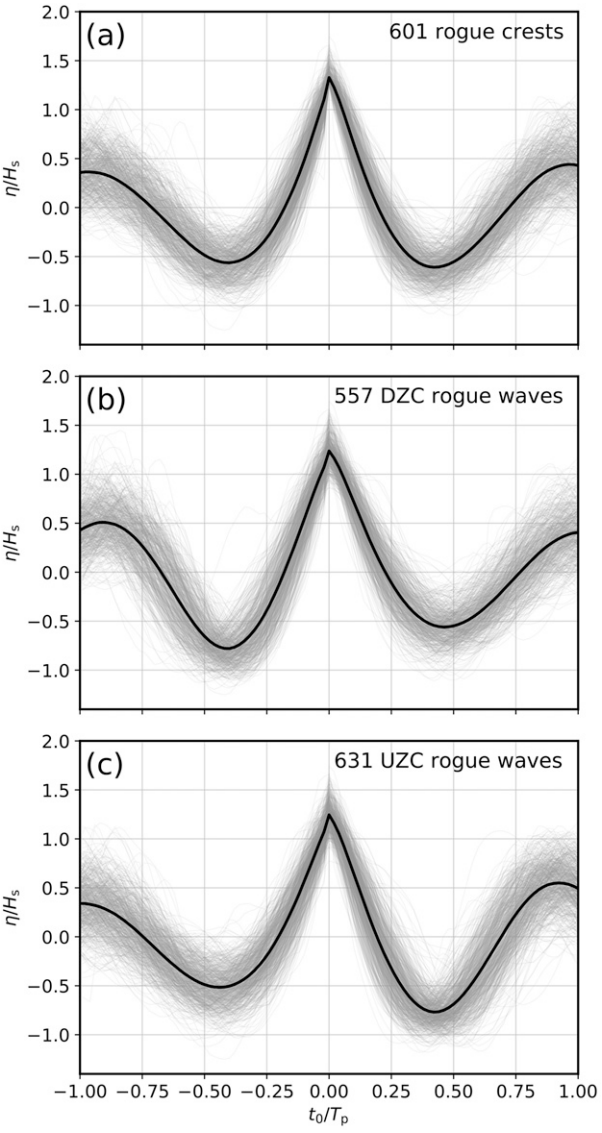

FIG. 2. (a) Temporal profiles of all verified rogue wave crests ($C/H_s \geq 1.25$) in the LASAR dataset. The individual crest profiles are plotted in gray, and the ensemble average profile is shown on top in black. (b),(c) The corresponding profiles of all verified downward zero-crossing (DZC) and upward zero-crossing (UZC) rogue waves ($H/H_s \geq 2.0$), respectively. In all panels, the surface elevations η on the vertical axes are normalized by the significant wave height H_s of that 20-min period, and the horizontal axes denote time centered on the maximum crest elevation ($t_0 = 0$) normalized by the prevailing peak wave period T_p.

wave heights, although the majority of the maximum wave steepness estimates lie considerably below the breaking-limiting threshold, supporting previous observations of wave breaking commencing at lower values of overall wave steepness than predicted by theoretical limits (Holthuijsen and Herbers 1986; Schwendeman and Thomson 2017). The triangular markers for maximum wave heights from the stereo video dataset in Figs. 3b and 3c represent space–time maximum wave heights, estimated

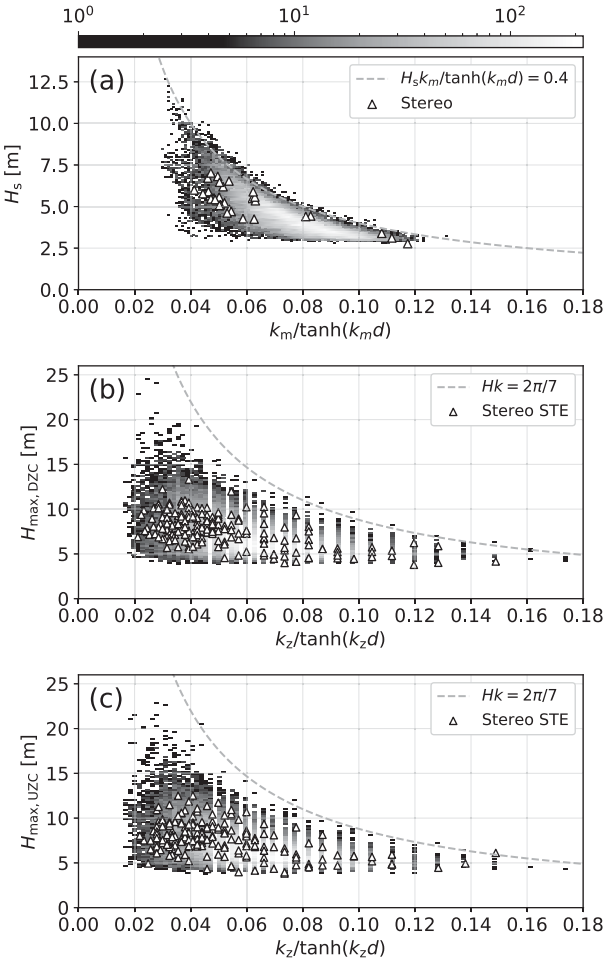

FIG. 3. (a) The significant wave height H_s is plotted against the depth-corrected spectral mean wavenumber $k_m/\tanh(k_m d)$ for each 20-min sea state in the LASAR dataset (shaded histogram). The shading indicates the density of the bin-averaged data. Corresponding values for individual sea states included in the stereo video dataset are marked with triangles. (b),(c) The maximum DZC and UZC wave heights per sea state $H_{\max}$ vs the local zero-crossing wavenumbers k_z estimated via the linear dispersion relation from the zero-crossing wave periods T_z. The triangles mark the space–time extreme (STE) wave heights from the stereo video dataset. The dashed curve in (a) is the bulk breaking-limited steepness threshold reported by Zippel and Thomson (2017) [Eq. (25)], and the dashed curves in (b) and (c) indicate the Stokes–Miche breaking-limited steepness limit for individual waves [Eq. (26)].

from time series of the maximum crest elevation detected in a 3600-m^2 sea surface area over time periods of $20T_m$ length. Space–time extreme crest statistics and dynamics are analyzed in more detail in sections 4d and 5.

b. *LASAR sea state characteristics versus skewness and kurtosis*

The estimation of wave height from a space–time field, such as a stereo video reconstruction, is relatively ambiguous due to the short-crested characteristics of real world wave fields (Fedele 2012). Likewise, the accurate estimation of wave height from a point time series assumes, perhaps unrealistically, that the wave shape evolves slowly enough that the zero-crossing points, which are measured a wave period apart in time, are representative of the true, instantaneous zero crossings by which the wavelength is defined. Due to these limitations, the remainder of the analysis herein will focus on extreme wave crests, which are more straightforward to define in both space and time.

Figure 4 illustrates the differences between the skewness and kurtosis as descriptors of the tail end of crest height distributions. The skewness γ and excess kurtosis $\kappa - 3$ were computed for each 20-min LASAR record, and are plotted in Fig. 4 against varying high percentiles of the corresponding 20-min crest height distributions. We observe that the skewness (left column of Fig. 4) has a finite and relatively consistent positive linear correlation (quantified with Pearson's correlation coefficient r_P) with crest height percentiles ranging from the 90th percentile (Fig. 4a) to the maximum crest height $C_{\max}$ (Fig. 4g). Curiously, the correlation for the skewness appears to peak at the 99th percentile (Fig. 4e) rather than at $C_{\max}$.

The linear correlation is more variable for percentiles of C against the excess kurtosis (right column of Fig. 4). This is most likely a consequence of the definition of the kurtosis as the fourth centralized moment, meaning that very large deviations from the mean water level (e.g., exceptionally high crests) are given proportionately much higher weight than small deviations (lower crests). For the 90th percentile (Fig. 4b), the correlation is nearly zero, whereas the correlation increases (i.e., becomes more positive) with increasing crest height percentile and peaks at $C_{\max}$. For both the skewness and the kurtosis, we also observe an increased scatter in the relationships with increasing percentile of crest height. The largest scatter observed in Figs. 4g and 4h may be a reflection of the fact that the skewness and kurtosis are descriptors of the shapes of the overall distributions, while the maximum crest height $C_{\max}$ comprises merely one realization from the distributions.

Figure 5 compares the distributions of the three spectral parameters used for assessing a sea state's susceptibility to extreme wave events discussed in section 2—namely the spectral steepness ϵ, the one-dimensional Benjamin–Feir index (BFI), and the directional Benjamin–Feir index (BFI$_{2D}$)—against the skewness and kurtosis. For the sea state skewness, an increasing relationship is observed for increased spectral steepness (Fig. 5a), in line with weakly nonlinear, second-order wave theory as indicated by the dashed curve representing the expression in Eq. (17). A somewhat weaker relationship is observed for skewness in terms of BFI and BFI$_{2D}$, as shown in Figs. 5b and 5c.

With regards to the sea state kurtosis, the correlation with any of the three sea state parameters is close to zero, implying that neither steepness nor BFI (including BFI$_{2D}$) alone is indicative of elevated probability of encountering an exceptionally high wave crest in a given sea state. This result is in contrast to the theoretical relationships for the sea state steepness and BFI [Eqs. (20)–(22)]; however, recall that these theoretical relations are only assumed to be valid for narrow-banded wave fields, whereas realistic storm sea states with high spectral steepness are known to be broad-banded in both frequency and

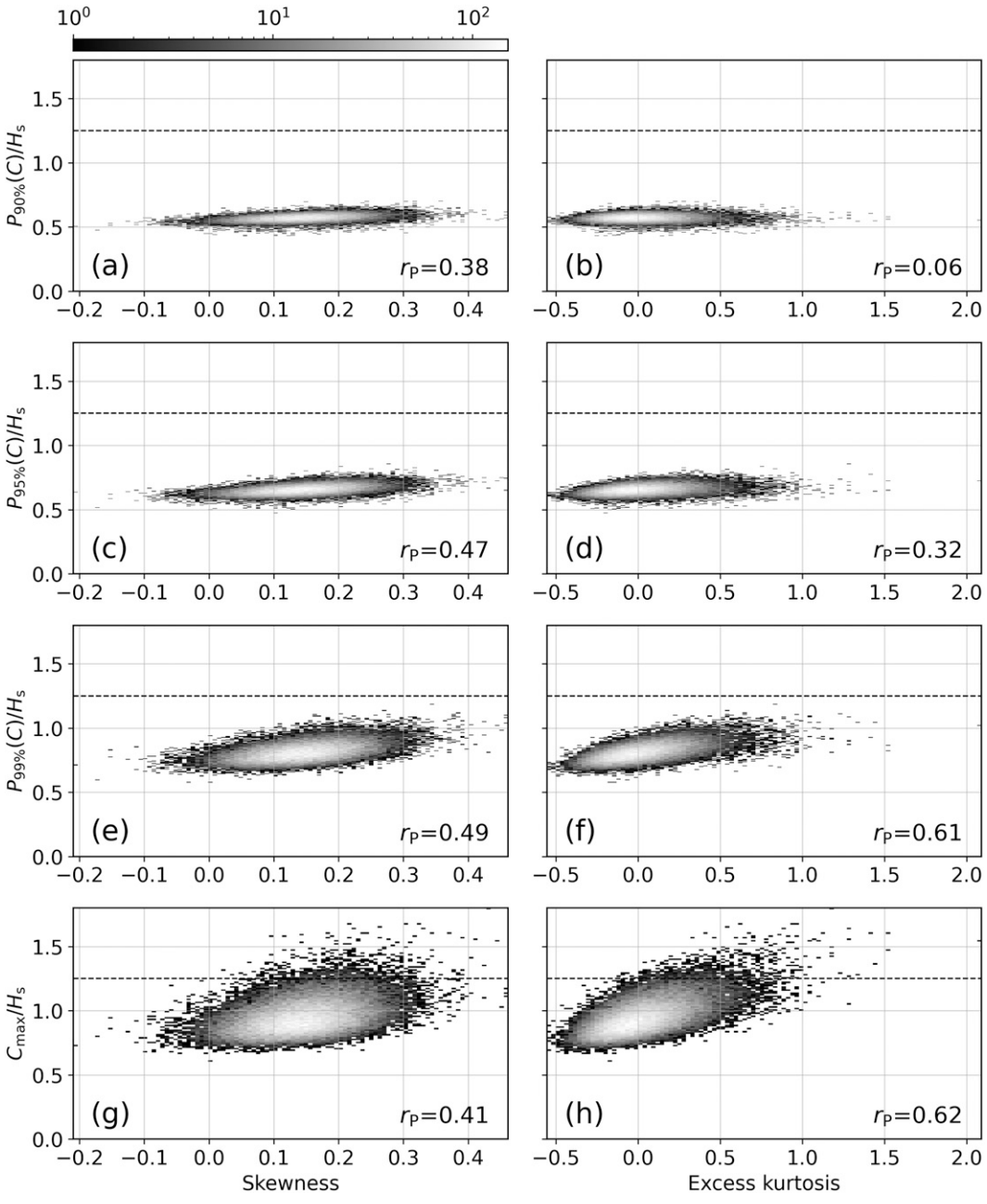

FIG. 4. Distributions of the (a),(b) 90th, (c),(d) 95th, (e),(f) 99th, and (g),(h) maximum percentiles of crest heights per sea state C, normalized by H_s, as functions of (left) the sea state skewness and (right) the sea state excess kurtosis in the LASAR dataset. The shading represents the density of data in each bin, and Pearson's linear correlation coefficients r_P are noted on each panel. The rogue crest threshold of $C_{max}/H_s = 1.25$ is marked with a horizontal dashed line in each panel.

directional spread (Donelan et al. 1985). The sea state duration is also held constant at 20 min throughout the entire dataset, which may cause a high bias for the kurtosis in young sea states with larger sample size (i.e., number of waves) due to shorter wave periods (Ponce de León and Guedes Soares 2014). Moreover, as discussed by Gramstad et al. (2018), the sample kurtosis κ is a biased estimator of the true population kurtosis, so that departures from the Gaussian value of $\kappa = 3$ are to be expected for wave records of limited length even for linear wave fields.

c. *LASAR crest height distributions at varying steepness and directional spread*

In this section, we examine the combined influence of steepness and directionality on the exceedance probability of crest

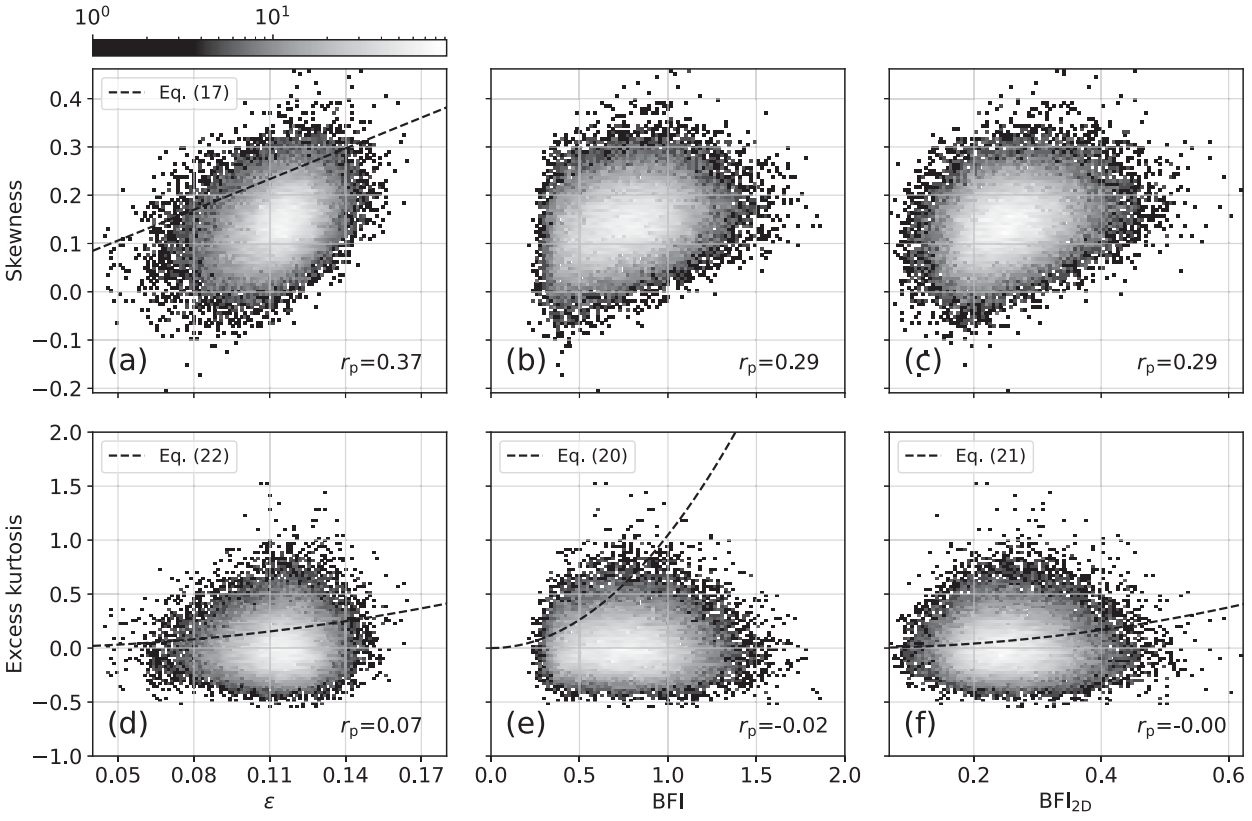

FIG. 5. Distributions of sea state (a)–(c) skewness and (d)–(f) excess kurtosis vs (left) spectral steepness ϵ, (center) the one-dimensional Benjamin–Feir index (BFI), and (right) the directional Benjamin–Feir index (BFI_{2D}). Pearson's correlation coefficients r_P are marked on each panel. The dashed curves show theoretical relations, the expressions of which can be found in the equations indicated by the legends.

heights for wind-sea-dominated sea states in the LASAR dataset. This investigation is motivated by the laboratory findings of Latheef and Swan (2013) and Karmpadakis et al. (2019), who found significant modulations of the tails of crest height distributions dependent on varying combinations of sea state steepness and directional spreading.

Wind-sea-dominated sea states are here defined in terms of the sea-swell energy ratio (SSER) (Petrova and Guedes Soares 2011),

$$\mathrm{SSER} = \frac{m_{0,\mathrm{ws}}}{m_{0,\mathrm{sw}}}, \tag{29}$$

where $m_{0,\mathrm{ws}}$ is the wind-sea variance and $m_{0,\mathrm{sw}}$ is the swell variance from the spectral partitioning of the WAM wave model used in the NORA3 hindcast [see Eq. (10.1) in ECMWF 2019]. We follow the definition used by Petrova and Guedes Soares (2011), where wind-sea-dominated sea states have SSER ≥ 1.6. The sea states are further grouped into subsets of varying spectral steepness with ranges of $\epsilon < 0.11$, $0.11 \leq \epsilon < 0.12$, $0.12 \leq \epsilon < 0.13$, and $\epsilon \geq 0.13$ and varying directional spreading with ranges of $\sigma_\theta < 30°$, $30° \leq \sigma_\theta < 35°$, $35° \leq \sigma_\theta < 40°$, and $\sigma_\theta \geq 40°$, where the steepness estimates are computed from the 1D LASAR spectra by Eq. (16) and the directional spread is estimated by Eq. (28) from the 2D NORA3 spectra.

The resulting crest height exceedance probability distributions normalized by the prevailing significant wave height H_s are shown in Fig. 6 alongside the theoretical Rayleigh distribution for linear crest heights [Eq. (3)] and the second-order distributions of Forristall (2000) and Tayfun (1980) [Eqs. (5) and (6)]. The second-order distributions have been estimated using the appropriate mean steepness and spectral bandwidth for each subset. The point clouds extending to slightly below the 10^{-2} probability level consist of the empirical exceedance probability distributions of each individual 20-min sea state. The large spread of these empirical distributions, reaching out both to the left and right of the theoretical distributions at probability levels below approximately 10^{-1}, is, most likely, mainly a reflection of the sampling variability inherent in point wave measurements in short-crested sea states (e.g., Bitner-Gregersen et al. 2020).

The crest heights in the individual sea states are also collapsed into composite distributions for each ϵ–σ_θ subset and plotted in Fig. 6 with black markers in order to facilitate the comparison of the distributions. Stability bands for the composite distributions are included with thin solid lines following Tayfun and Fedele (2007). The deviation of the composite distributions from the linear Rayleigh curve is obvious for all sea state subsets; however, more variability is observed in the accuracy of the second-order distributions

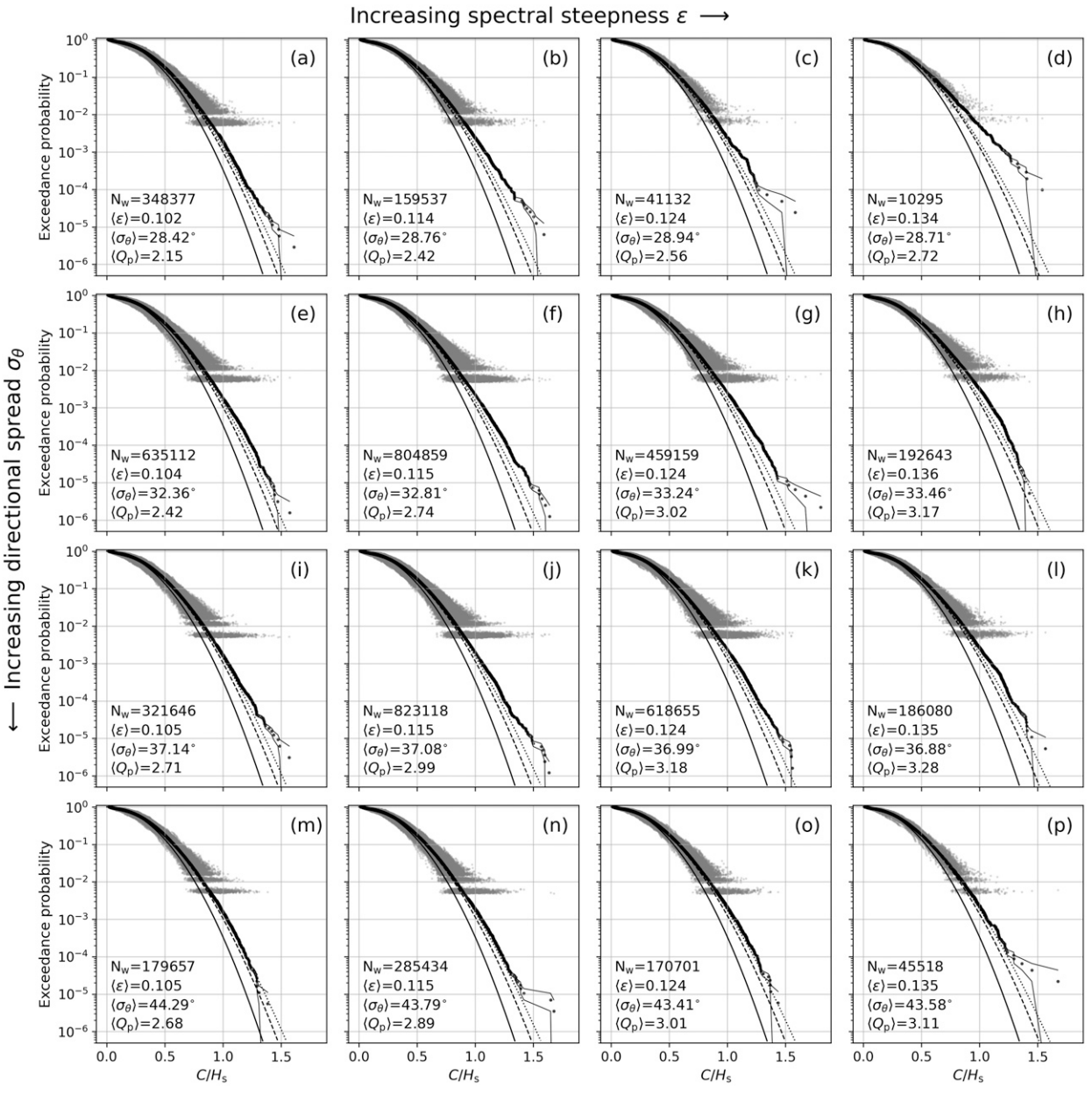

FIG. 6. LASAR normalized crest height exceedance probability distributions in wind-sea-dominated sea states with SSER ≥ 1.6, binned by column-wise increasing average spectral steepness ϵ, and row-wise increasing directional spread σ_θ. The point clouds marked by gray dots are the distributions of each individual 20-min sea state in the ϵ–σ_θ bins, and the black dots are the composite distributions of all sea states combined. The number of waves in each composite distribution N_w, as well as the bin-averaged steepness $\langle\epsilon\rangle$, directional spread $\langle\sigma_\theta\rangle$, and spectral peakedness $\langle Q_p\rangle$ are additionally annotated on each panel. The solid curves are the theoretical Rayleigh distributions for linear crests, and the dashed and dotted curves are the Forristall and Tayfun second-order crest height distributions for the bin-averaged steepness values, respectively.

in predicting the shapes of the distributions at low probabilities. Both second-order distributions underestimate the probability of encountering high wave crests to varying degree for narrow directional spread ($\sigma_\theta < 30°$; upper row of Fig. 6). The deviation of the empirical distributions from the second-order distributions in the narrow-spread sea states grows larger with increasing spectral steepness, suggesting the presence of higher-order nonlinear processes. The deviation appears most systematic in the high-steepness, narrow spreading subset of Fig. 6d. Somewhat less marked deviations from the second-order distributions are apparent also for more directionally spread sea states, especially at moderate and high average steepness. For low-to-moderate steepness and high directional spread (lowest row of Fig. 6),

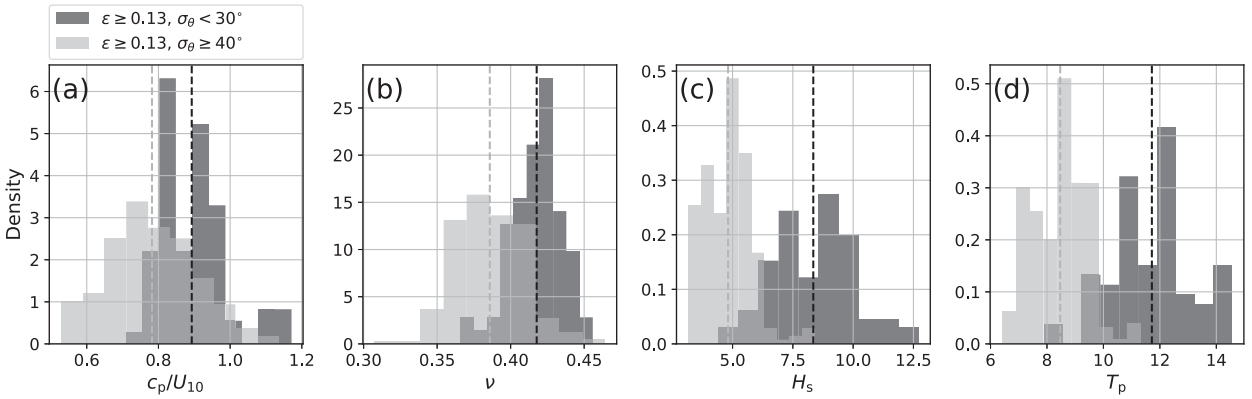

FIG. 7. Distributions of (a) wave age c_p/U_{10}, (b) spectral bandwidth ν, (c) significant wave height H_s, and (d) peak period T_p for high-steepness sea states with $\epsilon \geq 0.13$ and (dark bins) narrow directional spread with $\sigma_\theta < 30°$, corresponding to the crest height distribution shown in Fig. 6d, and (lighter bins) wide directional spread with $\sigma_\theta > 40°$, corresponding to the crest height distribution shown in Fig. 6p. The distribution means are marked with dashed vertical lines, and intersecting regions are colored with a medium dark shading.

the Tayfun distribution with bandwidth-adjusted steepness [Eq. (6)] predicts even the highest crest elevations to good accuracy, whereas the Forristall distribution [Eq. (5)] consistently underestimates the exceedance probabilities for large crest heights.

It is worth highlighting that there is a consistent increase in spectral peakedness (i.e., higher Q_p) with increasing steepness at each directional spread range, indicating a growing potential for high-order nonlinear effects (e.g., modulational instability). However, the peakedness also tends to increase somewhat with increasing directional spread. As discussed below and as shown in Fig. 7, this may be explained by the tendency of high directional spreading to coincide with developing sea states.

Focusing only on the high-steepness ($\epsilon \geq 0.13$) sea states with very narrow and very wide directional spread (Figs. 6d and 6p, respectively), we observe the aforementioned systematic deviation of the narrow-spread composite distribution from the second-order distributions, whereas the widely spread sea states display comparatively slight deviations for all but a small number of outliers. These results may at first seem to oppose our previous findings concerning the nonexistent correlation between the BFI and BFI_{2D} parameters and the sea state kurtosis (Fig. 5). However, a closer investigation of the corresponding LASAR frequency spectra, shown in Fig. 7, reveals that the two subsets contain widely different populations of sea states. The frequency bandwidth, quantified in terms of the bandwidth parameter ν (Fig. 7b), is markedly wider in the narrow-spread subset than in the broadly spread subset, implying weaker nonlinear modulational effects. Moreover, the narrow-spread subset is clearly composed of more mature sea states, as shown by the distributions of wave age c_p/U_{10} in Fig. 7a, with high H_s (Fig. 7c) and long T_p (Fig. 7d), whereas the broadly spread subset consists of younger, growing (potentially fetch or duration-limited) sea states with lower waves and shorter periods. The differences in spectral characteristics between these two subsets are discussed further in section 6.

d. *Space–time extreme crest heights from stereo video data*

In directionally spread seas, the probability of measuring a wave crest at its true wave-group apex with a point measurement such as a laser altimeter is in theory nil (see, e.g., Boccotti 2000). To address this limitation, we use the WASS wave-field reconstructions from the stereo video cameras nearly collocated with the LASAR instrument to investigate crest height statistics in a spatially and temporally resolved domain. In the left column of Fig. 8, we plot the highest normalized crest elevation C_{max}/H_s observed within regions of increasing area in the stereo video footprint during fixed time intervals $D = 20T_{m_{02}}$. The side lengths X and Y of the square sea surface areas are increased with increments of 1 m, resulting in a range of areas from 0 (a point measurement at the central stereo video grid cell) to 3600 m^2 (a 60 m × 60 m square centered around the point measurement). The varying areal extent results in sea state-dependent normalized time–space volumes of size $V_n = (XYD)/(L_x L_y T_{m_{02}})$, where the wave and crest lengths L_x and L_y, respectively, are estimated from the NORA3 spectra as described in section 2. The right column of Fig. 8 shows the variation of the ratio of observed and theoretical space–time (ST) extreme maximum crest heights to the temporal (T) extreme crest heights from the zero-area maximum crest heights.

In the left column of Fig. 8, we observe that the maximum normalized crest height increases with increasing space-time volume, consistent with the theory of space–time extremes (STE) (Baxevani and Rychlik 2006; Fedele 2012). Theoretical maximum expected linear crest heights (black curves) were estimated from the expanded maximum crest height distribution in Eq. (8) following Fedele (2012) as

$$\frac{\overline{C}_{max}}{H_s} = \zeta_0 + \frac{\gamma_E}{16\zeta_0 - F'\zeta_0/F(\zeta_0)}, \tag{30}$$

where $\gamma_E = 0.5772$ is the Euler–Mascheroni constant and ζ_0 satisfies

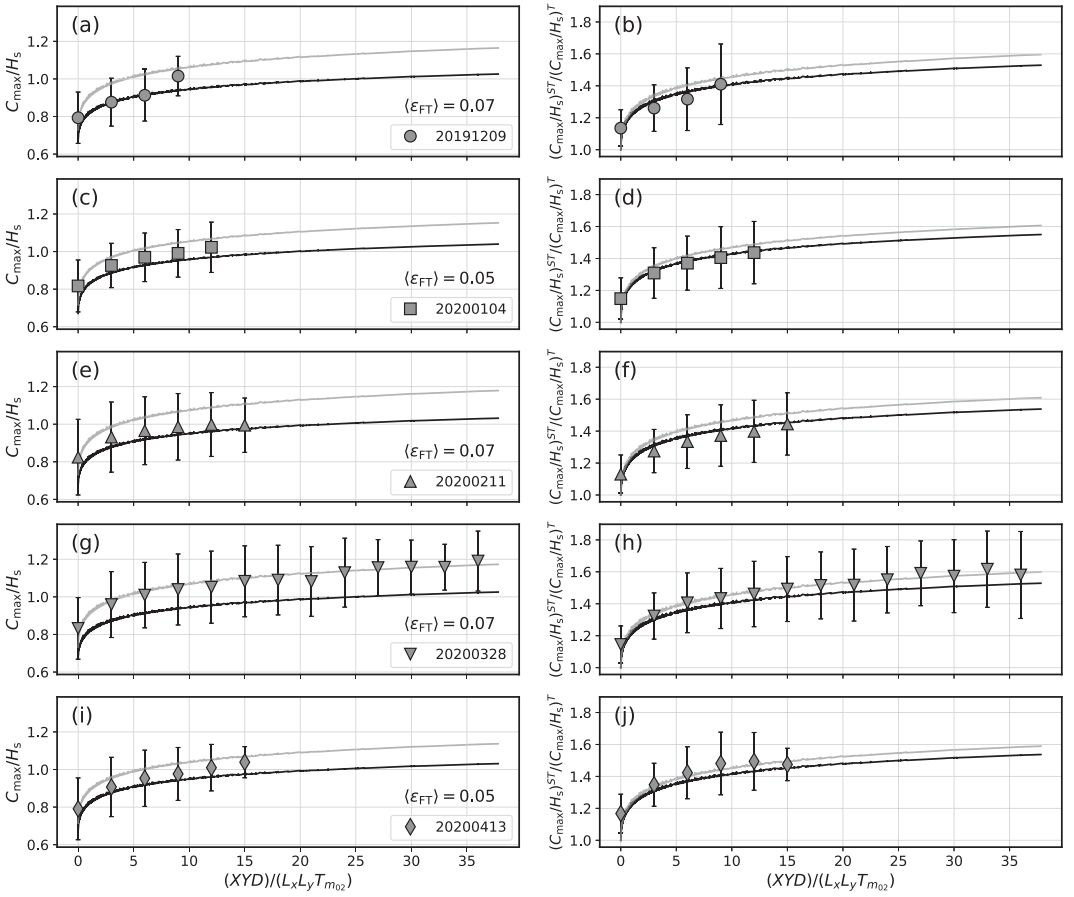

FIG. 8. (left) Variation of space–time extreme (STE) normalized crest heights from the 2019 to 2020 stereo video dataset as a function of the nondimensional space–time volume $V_n = (XYD)/(L_xL_yT_{m_{02}})$. The duration is fixed at $D = 20T_{m_{02}}$, and the sea surface area is increased from 0 (i.e., a point measurement) to 3600 m^2 (60 m × 60 m). The markers show bin averages of individual C_{max}/H_s data points, and each panel represents the separate acquisition dates. The error bars indicate confidence intervals based on one binned standard deviation. The black curve is the expected maximum crest height estimated by the Fedele (2012) 3D expansion of the Rayleigh crest height distribution, and the gray curve is the expected maximum crest height estimated by the expanded second-order Tayfun distribution following Benetazzo et al. (2015). (right) The corresponding change in the ratio of space–time (ST) extreme crest heights over the zero-area temporal (T) extremes for each STE segment. Note that the markers at $V_n = 0$ in the right column do not start at an ST–T ratio of 1 due to the bin averaging.

$$F(\zeta)\exp(-8\zeta^2) = 1, \quad \text{and} \tag{31}$$

$$F(z) = 16N_V\zeta^2 + 4N_S\zeta + N_B, \tag{32}$$

where N_V, N_S, and N_B are defined in Eq. (9). The corresponding second-order estimates of the maximum expected crest heights (gray curves) were computed based on Eq. (11) following Benetazzo et al. (2015) as

$$\frac{\overline{C}_{max}}{H_s} = \zeta_0 + 2\epsilon_{FT}\zeta_0^2 + \frac{\gamma_E(1 + 4\epsilon_{FT}\zeta_0)}{16\zeta_0 - F'(\zeta_0)/F(\zeta_0)}, \tag{33}$$

where ϵ_{FT} is the Fedele and Tayfun (2009) spectral steepness defined in Eq. (7). In each subplot, we have used the mean observed value $\langle\epsilon_{FT}\rangle$ (also specified on the subplots) to represent the sea state steepness of the theoretical second-order maximum crest height estimates. Furthermore, both the linear and second-order theoretical estimates were computed using mean values of the irregularity parameters, also listed in Table 3. In the majority of cases, the empirical maximum crest elevations are found to lie between the linear and second-

TABLE 3. Mean wave field irregularity parameters estimated from the NORA3 spectra for the stereo video STE sea states depicted in Fig. 8 (see also Table 2).

Date	$\langle\alpha_{xt}\rangle$	$\langle\alpha_{yt}\rangle$	$\langle\alpha_{xy}\rangle$
9 Dec 2019	0.81	−0.28	−0.11
4 Jan 2020	0.67	−0.38	−0.04
11 Feb 2020	0.82	0.09	0.05
28 Mar 2020	0.86	0.05	0.04
13 Apr 2020	0.83	−0.03	−0.02

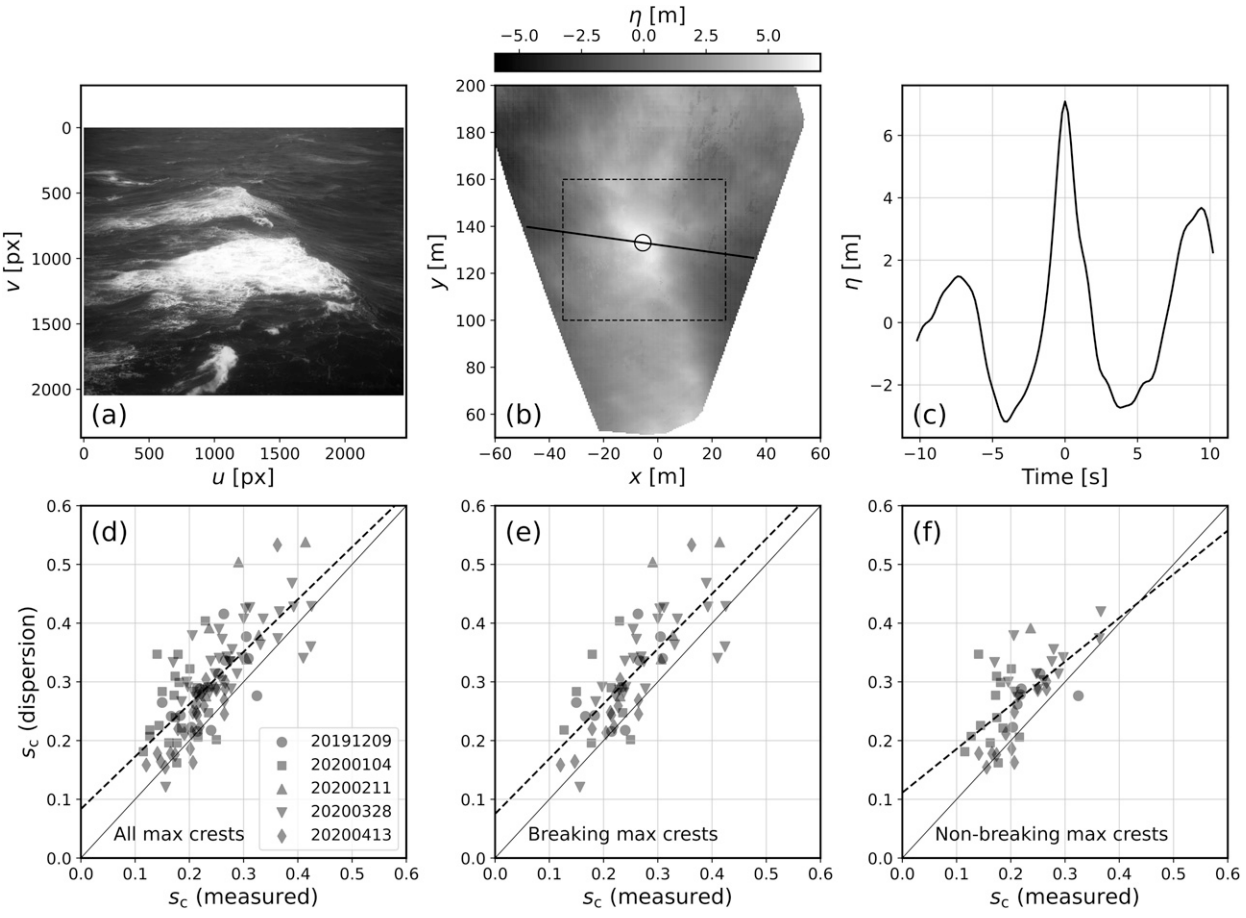

FIG. 9. (top) A sample space–time extreme (STE) maximum crest from 11 Feb 2020. The C_{max}/H_s ratio for the crest in question was 1.40 using the LASAR H_s estimate of 5.08, whereas using the WASS H_s estimate of 5.89 the ratio was 1.20. (a) The right-camera stereo video frame in its native projection at the moment of the maximum crest elevation. (b) The corresponding WASS-reconstructed sea surface grid with the STE maximum crest grid cell marked with a circle, and the across-crest transect line is shown with a solid line. The dashed region marks the maximum extent of the STE area. (c) Time series of the STE maximum crest grid cell in (b) centered on the maximum crest elevation time stamp. (bottom) Spatially measured crest steepness (x axes) vs crest estimated by dispersion from the temporal downward zero-crossing wave periods (y axes) for STE maximum crests in the 2019/20 stereo video STE dataset, shown (d) including all STE maximum crests for which the crest excursion length L_c can be resolved spatially, and (e),(f) with the maximum crests in (d) grouped into breaking and nonbreaking subsets, respectively.

order expected maxima, with the developing, moderately steep sea state of 28 March 2020 (Fig. 8g) most closely following the second-order theory.

As shown in the right column of Fig. 8, the observed STE/T ratios of the normalized maximum crest heights C_{max}/H_s are found to converge at a value of approximately 1.6 at the highest V_n values encountered in the stereo video data collected on 28 March 2020 (Fig. 8h). The other dates with stereo video acquisitions were characterized by more mature sea states with longer mean periods (see Table 1), leading to lower maximum values of V_n.

5. The shape and dynamics of space–time extreme crests

The STE maximum wave crests identified in the previous section allow for a direct measurement of their geometric steepness, forgoing the assumptions required for inferring the steepness from a point time series using the dispersion relation. For this analysis, only wave crests whose zero-sea level crossings at the moment of maximum crest elevation could be resolved spatially were included, reducing the sample size to 118 fully resolved wave crests. Unfortunately, the stereo video footprint is too small to cover the full dominant wavelength for most of the extreme crest cases encountered here. The 118 wave crests were further grouped into subsets of 69 breaking and 49 nonbreaking crests based on visual inspection of the original image frames with the WASS reconstructed sea surface mesh overlaid. However, in many cases the breaking classification was found to be somewhat ambiguous because of the wide range of spatial breaking scales present in the images inspected. The breaking/nonbreaking classification should, therefore, be taken as a rather subjective assessment. An example of a frame containing an unquestionably breaking maximum crest is shown in Fig. 9a.

The spatially resolved crest excursion length L_c (i.e., approximately half wavelength) was measured with transect lines across the wave crest defined such that the grid cell containing the STE maximum crest elevation was passed through, as depicted in Fig. 9b. The transect angle was taken as the mean wave direction from the WAMOS 2D spectrum, which was found to approximate the frame-wise trajectory of the STE maximum wave crests with good accuracy. The local crest steepness s_c of the STE maximum crests at focus (i.e., maximum amplitude) was then estimated following Banner et al. (2014) as

$$s_c = \frac{\pi}{L_c} C_{\max}, \tag{34}$$

where π/L_c is an estimate of the local crest wavenumber.

To compare the geometrically measured crest steepness against crest steepness estimated from time series using the linear dispersion relation, we first computed the downward zero-crossing wave period T_z from the time series of the grid cell containing the STE maximum crest (Fig. 9c). The zero-crossing period T_z was then used to estimate the wavelength L_z using the linear dispersion relation [Eq. (2)]. The crest excursion length was estimated from the ratio of the measured crest period T_{zc} to the measured trough period T_{zt} as

$$L_{c,\mathrm{disp}} = \frac{T_{zc}}{T_{zt}} L_z. \tag{35}$$

The crest steepness was then estimated from $L_{c,\mathrm{disp}}$ using Eq. (34).

As shown in Figs. 9d–f, the crest steepness estimated from dispersion is systematically higher than the geometrically measured crest steepness. This also holds for the breaking/nonbreaking subsets, with the distinction that the maximum observed crest steepness is somewhat higher in the breaking subset. The highest crest steepness estimated from dispersion is roughly 0.55, which is also the value reported by Toffoli et al. (2010a) for their observed maximum crest steepness in laboratory and field measurements using time series measurements combined with a second-order dispersion relation. However, the highest geometrically measured steepness of our breaking crests (Fig. 9e) is roughly 0.43, which is in line with the classical Stokes steepness limit of 0.44 (Michell 1893). The maximum crest steepness in our STE dataset is, therefore, overestimated by approximately 25% when using time series measurements combined with linear dispersion.

We suggest that a possible explanation for the discrepancy between the dispersive and geometric estimates of crest steepness is the universal crest speed slowdown of focused nonlinear wave groups discussed at length by Banner et al. (2014). A slowing down of the crest speed compared to the linear phase speed estimate, or a higher-order estimate thereof as in Eq. (27), would naturally lead to an underestimation of the crest excursion length $L_{c,\mathrm{disp}}$ and, consequently, an overestimation of the crest steepness. To investigate whether the STE maximum wave crests in the stereo video dataset experience a slowdown in crest speed, we plot the temporal evolution of the ensemble averaged STE across-crest transect profiles in Fig. 10. As shown in the upper row of Fig. 10, the average spatial profiles (plotted with the along-transect distance centered on the maximum crest elevation and normalized by the local wavelength L_z estimated from the temporal zero crossings T_z as the x axis) exhibit the characteristic asymmetric shape evolution of nonlinear wave groups described by Banner et al. (2014), where the leading wave front leans forward as the crest approaches the wave group focus (i.e., the crest profile snapshots approaching from the left) assumes a symmetric shape at focus, and continues propagating with an opposite, backward-leaning shape after focusing.

The normalized time–space diagrams of the ensemble average profiles in the lower row of Fig. 10 suggest that this shape evolution is accompanied by a deceleration and subsequent acceleration of the crest propagation speed just prior to and just after the moment of focusing. This crest speed reduction is implied by the steeper slope of the highest crest elevation contours (which mark the $\eta/H_s \geq 0.75$ level) compared to the white dashed diagonals representing the dispersive crest speed deduced from the downward zero-crossing period T_z and the crest excursion length L_z estimated from T_z using linear dispersion. Furthermore, judging by Figs. 10e and 10f, the slowdown signal is present in the average profiles of both breaking and nonbreaking STE maximum crests.

To quantify the apparent crest speed slowdown implied by Fig. 10, we calculated the ratio of the ensemble average crest propagation speed c to the corresponding linear phase speed c_0 by linear regressions of subsets of x_0/L_z–t_0/T_z grid cells whose normalized elevation η/H_s exceeds a minimum contour threshold. The slope coefficients of the linear regressions provide an estimate of the slope of the contour lines in x_0/L_z–t_0/T_z space. The regressions were focused on the main crest region bounded by the two outermost dashed white diagonals in Figs. 10d–f, and the inverse regression slopes were taken to approximate the c/c_0 ratios. As shown in Fig. 11a, the c/c_0 ratios thereby estimated for the ensemble average of all STE maximum wave crests are very close to 1 when estimated for large crest regions with $\eta/H_s \geq 0.5$. As one focuses in on the contours close to maximum crest elevation ($\eta/H_s \geq 0.75$), the c/c_0 ratio falls down to a minimum of approximately 0.76, indicating that the crest speed slowdown is highly focused near the moment of wave group focusing. The evolution is also very consistent between the crest speeds of all (solid lines), breaking (dashed lines) and nonbreaking (dotted lines) average STE crest transects.

In Fig. 11b, the crest speed evolution of the ensemble average STE wave crests is estimated by an alternative method, in which the local time–space gradient of the trajectory of the highest normalized sea surface elevation η/H_s at each time instant in the time–space diagrams of Figs. 10d–f is used to approximate the c/c_0 ratio as a function of the local crest steepness s_c [Eq. (34)]. The local trajectory gradient was estimated at different points in time before, during, and after crest focusing, represented in Fig. 11b with round markers of increasing (decreasing) size before (after) the moment of maximum crest elevation (and consequently, maximum crest steepness s_c), which is marked with triangles. Similarly to the

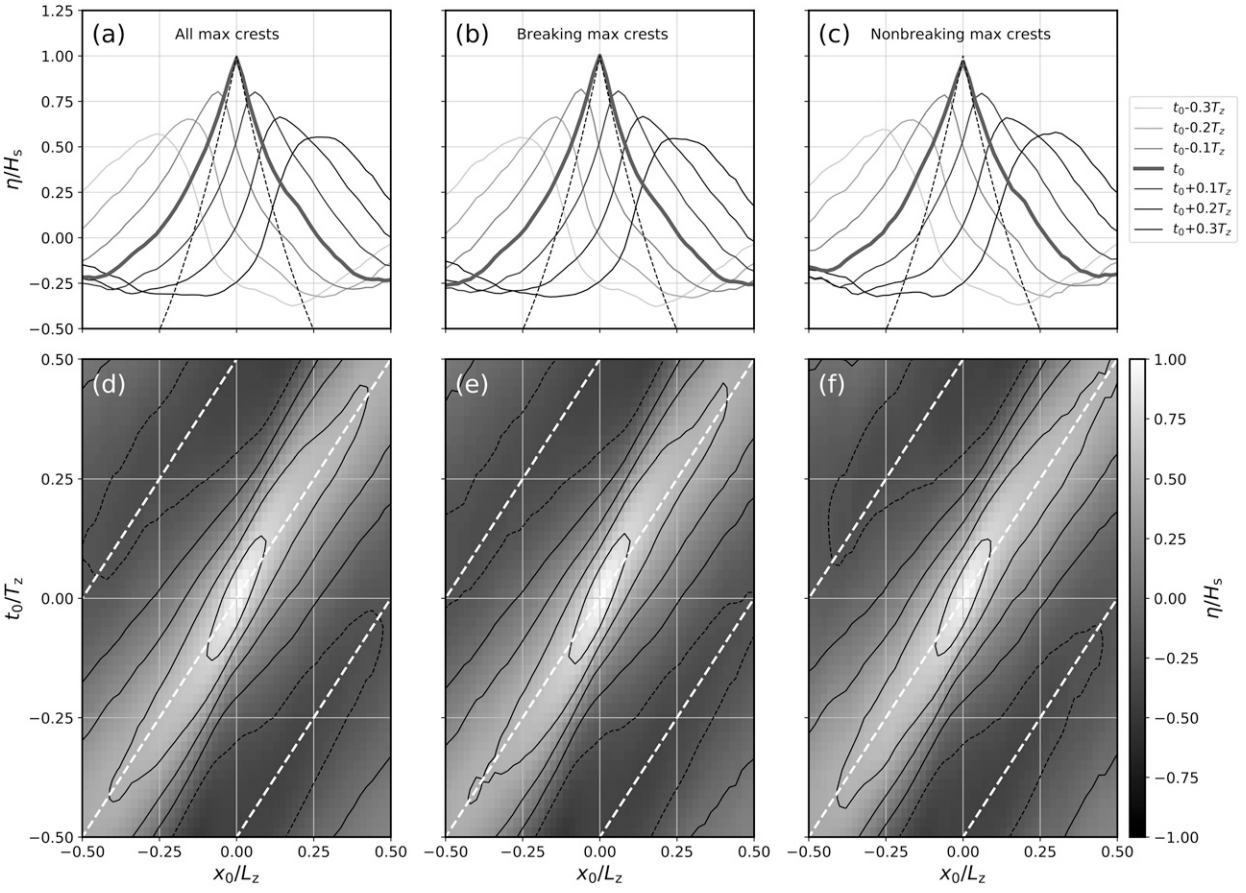

FIG. 10. Ensemble-averaged maximum across-crest profiles from the 2019 to 2020 stereo video STE dataset. (a)–(c) Average spatial transects before ($t_0/T_z < 0$), during ($t_0/T_z = 0$), and after ($t_0/T_z > 0$) the maximum average crest elevation for all average crest profiles in (a) and breaking and nonbreaking crest profiles in (b) and (c), respectively. The dashed profiles are the limiting Stokes crest profiles as given by Rainey and Longuet-Higgins (2006). (d)–(f) Space–time transects of the average crest profiles in (a)–(c), where the spatial axis is centered on the maximum crest location x_0 and normalized by the wavelength L_z estimated by dispersion from the temporal downward zero-crossing period of the average profile, T_z, and the time axis is centered on the maximum crest instant, t_0, and normalized by T_z. The black dashed (negative) and solid (positive) contour curves describe the η/H_s levels −0.25, 0, 0.25, 0.5, and 0.75, and the white dashed diagonals are the one-to-one linear dispersion lines for L_z/T_z of the ensemble average profiles.

slope of the linear regression, the local time–space gradient is inversely related to the c/c_0 ratio. Because the gradient is a local measure, the variability in estimated c/c_0 ratios is larger than with the linear regression method shown in Fig. 11a. However, the main result is consistent; that is, the crest speed ratio decreases from very near the linear estimate down to approximately 0.76 at maximum steepness (i.e., crest focus), before accelerating back to the linear estimate. The local crest speed evolution with varying crest steepness is also consistent between the average profiles of all, both breaking and nonbreaking, STE crests. It is also noteworthy that a second-order estimate of the phase speed [Eq. (27); marked with a dash-dotted line in Fig. 11b] predicts an increase of the crest speed with increasing steepness, which leads to an even larger disparity compared to the observed values at high values of crest steepness, as was also pointed out by Banner et al. (2014). The relatively high observed c/c_0 estimates at low-to-medium crest steepness in Fig. 11b should be interpreted with some caution, as those regions are less well sampled than the maximum crest regions due to the limited footprint size of the stereo video grids.

6. Discussion

A key question in rogue and extreme wave analysis is whether extraordinarily large wave crests form, in some sense, a unique population that is distinct from "normal" wave crests. Our distributions of maximum wave steepness deduced from point time series using linear dispersion (Fig. 3) show that even the steepest extreme waves remain effectively bounded by the classical Stokes–Miche limit based on the breaking-constrained Stokes (1847) wave profile (Miche 1944). Moreover, our analysis of the geometrically measured steepness of space–time extreme crests in section 5 suggests that the estimation of crest steepness using the zero crossing period of a time series combined with linear dispersion may in fact

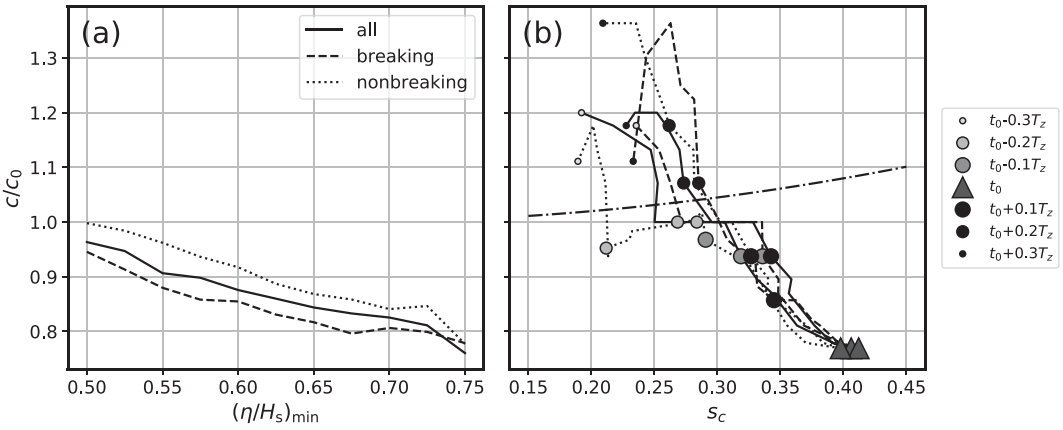

FIG. 11. Observed ratios of the measured crest speeds c against linear phase speeds c_0 estimated from the temporal zero crossings of the ensemble-averaged crest profiles in Fig. 10. (a) Crest speed ratios inferred from linear regressions to the space–time crest profiles thresholded at varying levels of η/H_s. The solid lines correspond to crest speed ratios estimated from all ensemble-averaged crest profiles in Fig. 10a, while the dashed and dotted lines are from the breaking and nonbreaking profiles in Figs. 10b and 10c, respectively. In (b), the c/c_0 ratios are inferred from local gradients of the ensemble average crest trajectories at varying time instants before, during and after the maximum crest elevation, and plotted against the local measured crest steepness s_c at each time instant. The dash-dotted line in (b) is the theoretical second-order nonlinear Stokes wave phase speed as reported in Banner et al. (2014).

overestimate the crest steepness by up to 25%. This result casts doubt on the findings of Toffoli et al. (2010a), who found, using time series data, that maximum breaking-limited crest steepness may exceed the Stokes–Miche limit by approximately 25%.

We contend that the seeming violation of the Stokes–Miche limit in maximum crest steepness measurements from time series may be explained by the crest speed slowdown at wave group focus experienced by wave crests in realistic, nonlinear wave fields (Banner et al. 2014), as verified in an average sense by our stereo video measurements (Fig. 11). Our confidence in this result is strengthened by the close correspondence of our observed crest speed slowdown of approximately 80% of the linear phase speed with previously published values (Banner et al. 2014; Fedele 2014; Schwendeman and Thomson 2017; Fedele et al. 2020). To our knowledge, ours are the first reported field measurements to show that the crest slowdown is inherent in both breaking and nonbreaking extreme wave crests. Similarly to the studies of Banner et al. (2014) and Schwendeman and Thomson (2017), however, our result is based on a fairly limited sample size of approximately 100 STE wave crests. To conclusively state whether the crest speed slowdown is a general feature of extreme wave crests, future studies may take advantage of the growing repositories of publicly available stereo video data (e.g., Guimarães et al. 2020).

In sea states characterized by high steepness, the shape and amplitude of the largest crests is known to be influenced by the competing effects of nonlinear amplification and wave breaking (Karmpadakis 2018). Figure 6 suggests that the impact of the sea state steepness is further complicated by wave field directionality, with deviations from second-order theory becoming more pronounced with increasing steepness and narrowing directional spread, echoing the laboratory findings of Latheef and Swan (2013) and Karmpadakis et al. (2019). This finding suggests that the sea state steepness alone may not be a sufficient parameter for determining the susceptibility of a sea state to an elevated probability of producing extreme crest elevations, as is assumed in standard second-order theories (Tayfun 1980; Forristall 2000). Instead, it seems apparent that the effects of wave field directionality should be incorporated into theoretical distributions alongside steepness.

The relative importance of higher than second-order nonlinear effects in realistic sea states is difficult to measure in field observations due to the large number of confounding factors being simultaneously at play. While the high-steepness, narrow-spread composite crest height exceedance probability distribution shown in Fig. 6d clearly deviates from the theoretical second order distributions, the average frequency bandwidth of the corresponding sea states is somewhat larger ($\langle\nu\rangle = 0.418$) than the average frequency bandwidth of the high-steepness, high-spread distribution (Fig. 6p; $\langle\nu\rangle = 0.386$) for which the crest elevations approximately follow the Tayfun distribution. At first glance, this may be taken to indicate that third-order nonlinear effects should be relatively weakened by the elevated frequency bandwidth in the narrow-directional sea states. Whether this difference in frequency bandwidth is large enough to offset the effects due to the differences in average directional spreading can be evaluated with the R parameter of Eq. (19). The high-directional spread sea states have an average value of $\langle R\rangle = 0.986$, which is nearly outside the $0 \leq R < 1$ range considered favorable for nonlinear energy focusing by Janssen and Bidlot (2009). The narrow-directional sea states, on the other hand, have an average value of $\langle R\rangle = 0.600$, well within the focusing regime. It is, therefore, plausible that nonlinear effects due to modulational instability are at least partially responsible for the large deviation from second-order

theory in the distribution of Fig. 6d. However, while the 70-m water depth at Ekofisk ensures that these sea states remain above the $k_p d = 1.36$ limit at which finite water depth inhibits modulational instability, the water depth is still shallow enough that intermediate-depth weakening of modulational effects most likely cannot be fully neglected (Janssen and Onorato 2007).

Figure 7 suggests that the shape of the tail of crest height distributions at high steepness is influenced not only by directionality, but also by wave age. As discussed by Donelan and Magnusson (2005), the breaking of dominant waves (i.e., waves at scales near the spectral peak) is modulated strongly by the maturity of the sea state. Based on the results of Donelan et al. (1985), in sea states approaching full development (e.g., Fig. 6d) dominant waves are expected to break only at very high amplitudes, whereas dominant wave breaking occurs at lower wave heights in strongly forced, developing sea states (e.g., Fig. 6p). The obvious departure from second-order predictions observed at high steepness, narrow spread, and mature wave age may therefore also be a consequence of reduced breaking of the largest, dominant wave crests compared to the more directionally spread, developing sea states in which dominant wave breaking is expected to be more widespread.

7. Conclusions

A novel dataset of quality controlled sea surface displacement measurements containing approximately 7 million individual waves, acquired by an array of four collocated laser altimeters (LASAR) in the central North Sea, has been used to investigate the role of sea state steepness and directionality on the characteristics of extreme wave crests. Our main conclusions from the analysis of this long-term point time series are summarized below.

Even the most extreme waves and wave crests identified in the LASAR dataset are "well behaved" in the sense that their shape (in terms of amplitude and wavelength) is effectively constrained by the breaking-limited steepness limit of Miche (1944).

While the presence of extreme individual wave crests within a wave record is by definition associated with elevated kurtosis, traditionally employed sea state parameters for indicating dangerous sea states, such as spectral steepness and the Benjamin–Feir index, are largely uncorrelated with high kurtosis, supporting previous findings that single sea state parameters are insufficient for predicting extreme wave crest elevations (e.g., Christou and Ewans 2014).

In wind-sea-dominated sea states, moderate-to-high sea state steepness coupled with narrow directional spreading is linked to the most systematic deviations of extreme crest height probabilities from standard second-order predictions. If the frequency bandwidth and the directional spread are sufficiently narrow, third-order modulational instability has been recognized as a potential mechanism responsible for significant deviations from second order theory. Wave age may also influence the shape of the tail of crest height distributions at high steepness by modulating the breaking probability of the highest wave crests, as discussed by Donelan and Magnusson (2005).

In addition to the long-term altimeter time series, approximately 10 h of stereo video-based space–time sea surface reconstructions from the same location have been analyzed for areal effects on measured crest heights and crest speed dynamics of space–time extreme crests. The main conclusions from this analysis are summarized below.

Space–time extreme (STE) crest elevations in a wide range of sea state conditions spanned by the stereo video dataset are shown to agree with linear expected maximum crest height estimates as defined by Fedele (2012), especially for small dimensionless space-time volume and moderate sea state steepness. For elevated steepness and larger space–time volumes, the second-order maximum expected crest heights as defined by Benetazzo et al. (2015) are found to estimate the observed STE crest elevations to good accuracy.

The STE wave crests identified in the stereo video dataset experience a distinct slowing down of the crest speed as the crests transform within the wave groups. The observed slowdown is highly localized in the region of the maximum crest elevation, where the average crest speed is approximately 80% of the linear dispersive phase speed. This observation is in line with previous field, laboratory, and numerical experiments of crest speed dynamics of breaking waves. However, our results show no apparent distinction between the crest speed dynamics of breaking and nonbreaking STE crests. This suggests that the crest speed slowdown is a ubiquitous characteristic of realistic weakly nonlinear deep-water wave groups in the ocean.

The slowdown of crest speeds at wave group focus may lead to an overestimation of the crest steepness of rogue or extreme waves from time series if the linear or second-order dispersion relation is used to estimate the crest speed. Moreover, taking into account the true, reduced wave steepness may result in an even greater deviation of observations from the second-order distributions of Tayfun (1980) and Forristall (2000) than what has been shown in the current study.

Acknowledgments. The authors gratefully acknowledge ConocoPhillips ASA and Equinor ASA for funding the StereoWave joint industry project (JIP). ØB acknowledges funding from the Research Council of Norway through the two projects StormRisk (Grant 300608) and ENTIRE (Grant 324227). This work could not be done with the enthusiastic support from Lars Bahr and Kjell Sandve at ConocoPhillips ASA and Einar Nygaard at Equinor ASA. In-house support at the Norwegian Meteorological Institute from Roger Storvik and Nico Budewitz was essential to getting the data archived and processed. The stereo video system was designed and built by Brian Scanlon.

Data availability statement. The NORA3 wave hindcast is archived and openly available on the THREDDS server of

the Norwegian Meteorological Institute (https://thredds.met.no/thredds/projects/windsurfer.html). The atmospheric hindcast (Haakenstad et al. 2021) is also openly available and archived at https://thredds.met.no/thredds/catalog/nora3/catalog.html. The quality-controlled LASAR dataset is openly available through the THREDDS server at https://thredds.met.no/thredds/catalog/stereowave/catalog.html.

REFERENCES

Adcock, T. A. A., and P. H. Taylor, 2014: The physics of anomalous ('rogue') ocean waves. *Rep. Prog. Phys.*, **77**, 105901, https://doi.org/10.1088/0034-4885/77/10/105901.

Adler, R. J., and J. E. Taylor, 2007: *Random Fields and Geometry*. Springer, 448 pp.

Banner, M., X. Barthelemy, F. Fedele, M. Allis, A. Benetazzo, F. Dias, and W. Peirson, 2014: Linking reduced breaking crest speeds to unsteady nonlinear water wave group behavior. *Phys. Rev. Lett.*, **112**, 114502, https://doi.org/10.1103/PhysRevLett.112.114502.

Barthelemy, X., M. L. Banner, W. L. Peirson, F. Fedele, M. Allis, and F. Dias, 2018: On a unified breaking onset threshold for gravity waves in deep and intermediate depth water. *J. Fluid Mech.*, **841**, 463–488, https://doi.org/10.1017/jfm.2018.93.

Baxevani, A., and I. Rychlik, 2006: Maxima for Gaussian seas. *Ocean Eng.*, **33**, 895–911, https://doi.org/10.1016/j.oceaneng.2005.06.006.

Benetazzo, A., 2006: Measurements of short water waves using stereo matched image sequences. *Coast. Eng.*, **53**, 1013–1032, https://doi.org/10.1016/j.coastaleng.2006.06.012.

——, F. Fedele, G. Gallego, P.-C. Shih, and A. Yezzi, 2012: Offshore stereo measurements of gravity waves. *Coast. Eng.*, **64**, 127–138, https://doi.org/10.1016/j.coastaleng.2012.01.007.

——, F. Barbariol, F. Bergamasco, A. Torsello, S. Carniel, and M. Sclavo, 2015: Observation of extreme sea waves in a space–time ensemble. *J. Phys. Oceanogr.*, **45**, 2261–2275, https://doi.org/10.1175/JPO-D-15-0017.1.

——, ——, ——, L. Bertotti, J. Yoo, J.-S. Shim, and L. Cavaleri, 2021: On the extreme value statistics of spatio-temporal maximum sea waves under cyclone winds. *Prog. Oceanogr.*, **197**, 102642, https://doi.org/10.1016/j.pocean.2021.102642.

Benjamin, T. B., and J. E. Feir, 1967: The disintegration of wave trains on deep water Part 1. Theory. *J. Fluid Mech.*, **27**, 417–430, https://doi.org/10.1017/S002211206700045X.

Bergamasco, F., A. Torsello, M. Sclavo, F. Barbariol, and A. Benetazzo, 2017: WASS: An open-source pipeline for 3D stereo reconstruction of ocean waves. *Comput. Geosci.*, **107**, 28–36, https://doi.org/10.1016/j.cageo.2017.07.001.

Bitner-Gregersen, E. M., O. Gramstad, A. K. Magnusson, and M. Malila, 2020: Challenges in description of nonlinear waves due to sampling variability. *J. Mar. Sci. Eng.*, **8**, 279, https://doi.org/10.3390/jmse8040279.

Boccotti, P., 2000: *Wave Mechanics for Ocean Engineering*. Elsevier, 520 pp.

Breivik, Ø., and Coauthors, 2022: The impact of a reduced high-wind Charnock coefficient on wave growth with application to the North Sea, the Norwegian Sea and the Arctic Ocean. *J. Geophys. Res. Oceans*, **127**, e2021JC018196, https://doi.org/10.1029/2021JC018196.

Carini, R. J., C. C. Chickadel, and A. T. Jessup, 2021: Surf zone waves at the onset of breaking: 2. Predicting breaking and breaker type. *J. Geophys. Res. Oceans*, **126**, e2020JC016935, https://doi.org/10.1029/2020JC016935.

Cattrell, A. D., M. Srokosz, B. I. Moat, and R. Marsh, 2018: Can rogue waves be predicted using characteristic wave parameters? *J. Geophys. Res. Oceans*, **123**, 5624–5636, https://doi.org/10.1029/2018JC013958.

Cavaleri, L., L. Bertotti, L. Torrisi, E. M. Bitner-Gregersen, M. Serio, and M. Onorato, 2012: Rogue waves in crossing seas: The Louis Majesty accident. *J. Geophys. Res.*, **117**, C00J10, https://doi.org/10.1029/2012JC007923.

——, F. Barbariol, and A. Benetazzo, 2020: Wind–wave modeling: Where we are, where to go. *J. Mar. Sci. Eng.*, **8**, 260, https://doi.org/10.3390/jmse8040260.

Christou, M., and K. Ewans, 2014: Field measurements of rogue water waves. *J. Phys. Oceanogr.*, **44**, 2317–2335, https://doi.org/10.1175/JPO-D-13-0199.1.

Dematteis, G., T. Grafke, M. Onorato, and E. Vanden-Eijnden, 2019: Experimental evidence of hydrodynamic instantons: The universal route to rogue waves. *Phys. Rev.*, **9**, 041057, https://doi.org/10.1103/PhysRevX.9.041057.

Donelan, M. A., and A. K. Magnusson, 2005: The role of meteorological focusing in generating rogue wave conditions. *Proc. 14th 'Aha Huliko'a Hawaiian Winter Workshop*, Honolulu, HI, University of Hawai'i at Mānoa, 139–145, https://www.soest.hawaii.edu/PubServices/2005pdfs/Donelan.pdf.

——, and ——, 2017: The making of the Andrea wave and other rogues. *Sci. Rep.*, **7**, 44124, https://doi.org/10.1038/srep44124.

——, J. Hamilton, and W. Hui, 1985: Directional spectra of wind-generated ocean waves. *Philos. Trans. Roy. Soc.*, **A315**, 509–562, https://doi.org/10.1098/rsta.1985.0054.

Dysthe, K., H. E. Krogstad, and P. Müller, 2008: Oceanic rogue waves. *Annu. Rev. Fluid Mech.*, **40**, 287–310, https://doi.org/10.1146/annurev.fluid.40.111406.102203.

Dysthe, K. B., K. Trulsen, H. E. Krogstad, and H. Socquet-Juglard, 2003: Evolution of a narrow-band spectrum of random surface gravity waves. *J. Fluid Mech.*, **478**, 1–10, https://doi.org/10.1017/S0022112002002616.

ECMWF, 2019: IFS Documentation CY46R1–Part VII: ECMWF wave model. ECMWF, 103 pp, https://www.ecmwf.int/node/19311.

Fedele, F., 2012: Space–time extremes in short-crested storm seas. *J. Phys. Oceanogr.*, **42**, 1601–1615, https://doi.org/10.1175/JPO-D-11-0179.1.

——, 2014: Geometric phases of water waves. *Europhys. Lett.*, **107**, 69001, https://doi.org/10.1209/0295-5075/107/69001.

——, 2015: On the kurtosis of deep-water gravity waves. *J. Fluid Mech.*, **782**, 25–36, https://doi.org/10.1017/jfm.2015.538.

——, and M. A. Tayfun, 2009: On nonlinear wave groups and crest statistics. *J. Fluid Mech.*, **620**, 221–239, https://doi.org/10.1017/S0022112008004424.

——, A. Benetazzo, G. Gallego, P.-C. Shih, A. Yezzi, F. Barbariol, and F. Ardhuin, 2013: Space–time measurements of oceanic sea states. *Ocean Modell.*, **70**, 103–115, https://doi.org/10.1016/j.ocemod.2013.01.001.

——, J. Brennan, S. Ponce de León, J. Dudley, and F. Dias, 2016: Real world ocean rogue waves explained without the modulational instability. *Sci. Rep.*, **6**, 27715, https://doi.org/10.1038/srep27715.

——, J. Herterich, A. Tayfun, and F. Dias, 2019: Large nearshore storm waves off the Irish coast. *Sci. Rep.*, **9**, 15406, https://doi.org/10.1038/s41598-019-51706-8.

——, M. L. Banner, and X. Barthelemy, 2020: Crest speeds of unsteady surface water waves. *J. Fluid Mech.*, **899**, A5, https://doi.org/10.1017/jfm.2020.424.

Forristall, G. Z., 2000: Wave crest distributions: Observations and second-order theory. *J. Phys. Oceanogr.*, **30**, 1931–1943, https://doi.org/10.1175/1520-0485(2000)030<1931:WCDOAS>2.0.CO;2.

Gemmrich, J., and C. Garrett, 2011: Dynamical and statistical explanations of observed occurrence rates of rogue waves. *Nat. Hazards Earth Syst. Sci.*, **11**, 1437–1446, https://doi.org/10.5194/nhess-11-1437-2011.

——, and L. Cicon, 2022: Generation mechanism and prediction of an observed extreme rogue wave. *Sci. Rep.*, **12**, 1718, https://doi.org/10.1038/s41598-022-05671-4.

——, C. J. Zappa, M. L. Banner, and R. P. Morison, 2013: Wave breaking in developing and mature seas. *J. Geophys. Res. Oceans*, **118**, 4542–4552, https://doi.org/10.1002/jgrc.20334.

Goda, Y., 1970: Estimation of the rate of irregular wave overtopping of seawalls. *Rep. Port Harbour Res. Inst.*, **9**, 3–41.

Gramstad, O., and K. Trulsen, 2007: Influence of crest and group length on the occurrence of freak waves. *J. Fluid Mech.*, **582**, 463–472, https://doi.org/10.1017/S0022112007006507.

——, E. M. Bitner-Gregersen, K. Trulsen, and J. C. Nieto Borge, 2018: Modulational instability and rogue waves in crossing sea states. *J. Phys. Oceanogr.*, **48**, 1317–1331, https://doi.org/10.1175/JPO-D-18-0006.1.

Guimarães, P. V., F. Ardhuin, F. Bergamasco, F. Leckler, J.-F. Filipot, J.-S. Shim, V. Dulov, and A. Benetazzo, 2020: A data set of sea surface stereo images to resolve space-time wave fields. *Sci. Data*, **7**, 145, https://doi.org/10.1038/s41597-020-0492-9.

Haakenstad, H., Ø. Breivik, B. Furevik, M. Reistad, P. Bohlinger, and O. J. Aarnes, 2021: NORA3: A nonhydrostatic high-resolution hindcast of the North Sea, the Norwegian Sea, and the Barents Sea. *J. Appl. Meteor. Climatol.*, **60**, 1443–1464, https://doi.org/10.1175/JAMC-D-21-0029.1.

Häfner, D., J. Gemmrich, and M. Jochum, 2021: Real-world rogue wave probabilities. *Sci. Rep.*, **11**, 10084, https://doi.org/10.1038/s41598-021-89359-1.

Haver, S., 2004: A possible freak wave event measured at the Draupner platform January 1 1995. *Proc. Rogue Waves 2004 Workshop*, Brest, France, IFREMER, 1–8.

Hersbach, H., and Coauthors, 2020: The ERA5 global reanalysis. *Quart. J. Roy. Meteor. Soc.*, **146**, 1999–2049, https://doi.org/10.1002/qj.3803.

Holthuijsen, L. H., 2007: *Waves in Oceanic and Coastal Waters*. Cambridge University Press, 387 pp.

——, and T. H. C. Herbers, 1986: Statistics of breaking waves observed as whitecaps in the open sea. *J. Phys. Oceanogr.*, **16**, 290–297, https://doi.org/10.1175/1520-0485(1986)016<0290:SOBWOA>2.0.CO;2.

Janssen, P. A. E. M., 2003: Nonlinear four-wave interactions and freak waves. *J. Phys. Oceanogr.*, **33**, 863–884, https://doi.org/10.1175/1520-0485(2003)33<863:NFIAFW>2.0.CO;2.

——, 2009: On some consequences of the canonical transformation in the Hamiltonian theory of water waves. *J. Fluid Mech.*, **637**, 1–44, https://doi.org/10.1017/S0022112009008131.

——, and M. Onorato, 2007: The intermediate water depth limit of the Zakharov equation and consequences for wave prediction. *J. Phys. Oceanogr.*, **37**, 2389–2400, https://doi.org/10.1175/JPO3128.1.

——, and J.-R. Bidlot, 2009: On the extension of the freak wave warning system and its verification. ECMWF Tech. Memo. 588, 42 pp., www.ecmwf.int/sites/default/files/elibrary/2009/10243-extension-freak-wave-warning-system-and-its-verification.pdf.

Johnson, D., 2002: *DIrectional WAve SPectra Toolbox Version 1.3*. MetOcean Solutions Ltd., https://github.com/metocean/diwasp.

Karmpadakis, I., 2018: Wave statistics in intermediate and shallow water depths. Ph.D. thesis, Civil and Environmental Engineering, Imperial College London, 284 pp., https://spiral.imperial.ac.uk/handle/10044/1/87397.

——, and C. Swan, 2020: On the average shape of the largest waves in finite water depths. *J. Phys. Oceanogr.*, **50**, 1023–1043, https://doi.org/10.1175/JPO-D-19-0165.1.

——, ——, and M. Christou, 2019: Laboratory investigation of crest height statistics in intermediate water depths. *Proc. Roy. Soc.*, **475A**, 20190183, https://doi.org/10.1098/rspa.2019.0183.

Kleiss, J. M., and W. K. Melville, 2010: Observations of wave breaking kinematics in fetch-limited seas. *J. Phys. Oceanogr.*, **40**, 2575–2604, https://doi.org/10.1175/2010JPO4383.1.

Krogstad, H. E., S. F. Barstow, J. P. Mathisen, L. Lønseth, A. K. Magnusson, and M. A. Donelan, 2008: Extreme waves in the long-term wave measurements at Ekofisk. *Proc. Rogue Waves 2008 Workshop*, Brest, France, Ifremer, 23–33, https://archimer.ifremer.fr/doc/00133/24444/.

Kuik, A. J., G. P. Van Vledder, and L. H. Holthuijsen, 1988: A method for the routine analysis of pitch-and-roll buoy wave data. *J. Phys. Oceanogr.*, **18**, 1020–1034, https://doi.org/10.1175/1520-0485(1988)018<1020:AMFTRA>2.0.CO;2.

Latheef, M., and C. Swan, 2013: A laboratory study of wave crest statistics and the role of directional spreading. Proc. Roy. Soc., **469A**, 20120696, https://doi.org/10.1098/rspa.2012.0696.

Longuet-Higgins, M. S., 1963: The effect of non-linearities on statistical distributions in the theory of sea waves. *J. Fluid Mech.*, **17**, 459–480, https://doi.org/10.1017/S0022112063001452.

——, 1975: On the joint distribution of the periods and amplitudes of sea waves. *J. Geophys. Res.*, **80**, 2688–2694, https://doi.org/10.1029/JC080i018p02688.

Lygre, A., and H. E. Krogstad, 1986: Maximum entropy estimation of the directional distribution in ocean wave spectra. *J. Phys. Oceanogr.*, **16**, 2052–2060, https://doi.org/10.1175/1520-0485(1986)016<2052:MEEOTD>2.0.CO;2.

Magnusson, A. K., and M. A. Donelan, 2013: The Andrea wave characteristics of a measured North Sea rogue wave. *J. Offshore Mech. Arctic Eng.*, **135**, 031108, https://doi.org/10.1115/1.4023800.

Makri, I. M., S. M. Rose, M. Christou, R. Gibson, and G. Feld, 2016: Examining field measurements of deep-water crest statistics. *Proc. ASME 2016 35th Int. Conf. on Ocean, Offshore and Arctic Engineering. Volume 7: Ocean Engineering*, American Society of Mechanical Engineers, V007T06A092, https://asmedigitalcollection.asme.org/OMAE/proceedings-abstract/OMAE2016/49989/V007T06A092/281031.

Malila, M. P., P. Bohlinger, S. Støle-Hentschel, O. Breivik, G. Hope, and A. K. Magnusson, 2022a: A non-parametric, data-driven approach to despiking ocean surface wave time series. *J. Atmos. Oceanic Technol.*, **39**, 71–90, https://doi.org/10.1175/JTECH-D-21-0067.1.

——, J. Thomson, Ø. Breivik, A. Benetazzo, B. Scanlon, and B. Ward, 2022b: On the groupiness and intermittency of oceanic whitecaps. *J. Geophys. Res. Oceans*, **127**, e2021JC017938, https://doi.org/10.1029/2021JC017938.

McAllister, M. L., S. Draycott, T. A. A. Adcock, P. H. Taylor, and T. S. van den Bremer, 2019: Laboratory recreation of the Draupner wave and the role of breaking in crossing seas. *J. Fluid Mech.*, **860**, 767–786, https://doi.org/10.1017/jfm.2018.886.

Mendes, S., A. Scotti, and P. Stansell, 2021: On the physical constraints for the exceeding probability of deep water rogue waves. *Appl. Ocean Res.*, **108**, 102402, https://doi.org/10.1016/j.apor.2020.102402.

Miche, A., 1944: Mouvements ondulatoires de la mer en profondeur croissante ou décroissante. Première partie. Mouvements ondulatoires périodiques et cylindriques en profondeur constante. *Ann. Ponts Chaussees*, **114**, 42–78.

Michell, J. H., 1893: On the highest waves in water. *London Edinburgh Dublin Philos. Mag. J. Sci.*, **36**, 430–437, https://doi.org/10.1080/14786449308620499.

Mori, N., and P. A. E. M. Janssen, 2006: On kurtosis and occurrence probability of freak waves. *J. Phys. Oceanogr.*, **36**, 1471–1483, https://doi.org/10.1175/JPO2922.1.

——, M. Onorato, P. A E. M. Janssen, A. R. Osborne, and M. Serio, 2007: On the extreme statistics of long-crested deep water waves: Theory and experiments. *J. Geophys. Res.*, **112**, C09011, https://doi.org/10.1029/2006JC004024.

——, ——, and P. A. E. M. Janssen, 2011: On the estimation of the kurtosis in directional sea states for freak wave forecasting. *J. Phys. Oceanogr.*, **41**, 1484–1497, https://doi.org/10.1175/2011JPO4542.1.

Perlin, M., W. Choi, and Z. Tian, 2013: Breaking waves in deep and intermediate waters. *Annu. Rev. Fluid Mech.*, **45**, 115–145, https://doi.org/10.1146/annurev-fluid-011212-140721.

Petrova, P. G., and C. Guedes Soares, 2011: Wave height distributions in bimodal sea states from offshore basins. *Ocean Eng.*, **38**, 658–672, https://doi.org/10.1016/j.oceaneng.2010.12.018.

Phillips, O. M., 1985: Spectral and statistical properties of the equilibrium range in wind-generated gravity waves. *J. Fluid Mech.*, **156**, 505–531, https://doi.org/10.1017/S0022112085002221.

Pleskachevsky, A. L., S. Lehner, and W. Rosenthal, 2012: Storm observations by remote sensing and influences of gustiness on ocean waves and on generation of rogue waves. *Ocean Dyn.*, **62**, 1335–1351, https://doi.org/10.1007/s10236-012-0567-z.

Ponce de León, S., and C. Guedes Soares, 2014: Extreme wave parameters under North Atlantic extratropical cyclones. *Ocean Modell.*, **81**, 78–88, https://doi.org/10.1016/j.ocemod.2014.07.005.

Power, H. E., M. G. Hughes, T. Aagaard, and T. E. Baldock, 2010: Nearshore wave height variation in unsaturated surf. *J. Geophys. Res.*, **115**, C08030, https://doi.org/10.1029/2009JC005758.

Rainey, R. C. T., and M. S. Longuet-Higgins, 2006: A close one-term approximation to the highest Stokes wave on deep water. *Ocean Eng.*, **33**, 2012–2024, https://doi.org/10.1016/j.oceaneng.2005.09.014.

Reichert, K., K. Hessner, J. C. Nieto Borge, and J. Dittmer, 1999: WaMoS II: A radar based wave and current monitoring system. *The Ninth Int. Offshore and Polar Engineering Conf.*, Brest, France, OnePetro, 1–5, https://onepetro.org/ISOPEIOPEC/proceedings-abstract/ISOPE99/All-ISOPE99/ISOPE-I-99-246/24940.

Saket, A., W. L. Peirson, M. L. Banner, and M. J. Allis, 2018: On the influence of wave breaking on the height limits of two-dimensional wave groups propagating in uniform intermediate depth water. *Coast. Eng.*, **133**, 159–165, https://doi.org/10.1016/j.coastaleng.2017.12.015.

Schwendeman, M. S., and J. Thomson, 2017: Sharp-crested breaking surface waves observed from a ship-based stereo video system. *J. Phys. Oceanogr.*, **47**, 775–792, https://doi.org/10.1175/JPO-D-16-0187.1.

Serio, M., M. Onorato, A. R. Osborne, and P. A. E. M. Janssen, 2005: On the computation of the Benjamin-Feir Index. *Nuovo Cimento*, **28C**, 893–903, https://doi.org/10.1393/ncc/i2005-10134-1.

Stokes, G. G., 1847: On the theory of oscillatory waves. *Trans. Cambridge Philos. Soc.*, **8**, 441–455.

Støle-Hentschel, S., K. Trulsen, L. Rye, and A. Raustøl, 2018: Extreme wave statistics of counter-propagating, irregular, long-crested sea states. *Phys. Fluids*, **30**, 067102, https://doi.org/10.1063/1.5034212.

Tayfun, M. A., 1980: Narrow-band nonlinear sea waves. *J. Geophys. Res.*, **85**, 1548–1552, https://doi.org/10.1029/JC085iC03p01548.

——, 1986: On narrow-band representation of ocean waves: 1. Theory. *J. Geophys. Res.*, **91**, 7743–7752, https://doi.org/10.1029/JC091iC06p07743.

——, and F. Fedele, 2007: Wave-height distributions and nonlinear effects. *Ocean Eng.*, **34**, 1631–1649, https://doi.org/10.1016/j.oceaneng.2006.11.006.

Thomson, J., and A. T. Jessup, 2009: A Fourier-based method for the distribution of breaking crests from video observations. *J. Atmos. Oceanic Technol.*, **26**, 1663–1671, https://doi.org/10.1175/2009JTECHO622.1.

Toffoli, A., A. V. Babanin, M. Onorato, and T. Waseda, 2010a: Maximum steepness of oceanic waves: Field and laboratory experiments. *Geophys. Res. Lett.*, **37**, L05603, https://doi.org/10.1029/2009GL041771.

——, O. Gramstad, K. Trulsen, J. Monbaliu, E. M. Bitner-Gregersen, and M. Onorato, 2010b: Evolution of weakly nonlinear random directional waves: Laboratory experiments and numerical simulations. *J. Fluid Mech.*, **664**, 313–336, https://doi.org/10.1017/S002211201000385X.

——, A. V. Babanin, M. A. Donelan, B. K. Haus, and D. Jeong, 2011: Estimating sea spray volume with a laser altimeter. *J. Atmos. Oceanic Technol.*, **28**, 1177–1183, https://doi.org/10.1175/2011JTECHO827.1.

Trulsen, K., J. C. Nieto Borge, O. Gramstad, L. Aouf, and J.-M. Lefèvre, 2015: Crossing sea state and rogue wave probability during the Prestige accident. *J. Geophys. Res. Oceans*, **120**, 7113–7136, https://doi.org/10.1002/2015JC011161.

Tucker, M. J., P. G. Challenor, and D. J. T. Carter, 1984: Numerical simulation of a random sea: A common error and its effect upon wave group statistics. *Appl. Ocean Res.*, **6**, 118–122, https://doi.org/10.1016/0141-1187(84)90050-6.

Vieira, M., P. V. Guimarães, N. Violante-Carvalho, A. Benetazzo, F. Bergamasco, and H. Pereira, 2020: A low-cost stereo video system for measuring directional wind waves. *J. Mar. Sci. Eng.*, **8**, 831, https://doi.org/10.3390/jmse8110831.

Voermans, J. J., A. V. Babanin, C. Kirezci, J. T. Carvalho, M. F. Santini, B. F. Pavani, and L. P. Pezzi, 2021: Wave anomaly detection in wave measurements. *J. Atmos. Oceanic Technol.*, **38**, 525–536, https://doi.org/10.1175/JTECH-D-20-0090.1.

WAMDI Group, 1988: The WAM model—A third generation ocean wave prediction model. *J. Phys. Oceanogr.*, **18**, 1775–1810, https://doi.org/10.1175/1520-0485(1988)018<1775:TWMTGO>2.0.CO;2.

Zippel, S., and J. Thomson, 2017: Surface wave breaking over sheared currents: Observations from the mouth of the Columbia River. *J. Geophys. Res. Oceans*, **122**, 3311–3328, https://doi.org/10.1002/2016JC012498.